NOVA SCHOOL OF SCIENCE & TECHNOLOGY

DEPARTAMENT OF MATERIAL SCIENCES

Francisco Silva Nunes Martins

BSc in Micro and Nanotechnology Engineering

Low-cost Smart Ink for Intelligent Packaging

Dissertation submitted in partial fulfillment of the requirements for the degree of Masters in Micro and Nanotechnologies Engineering

MASTER IN MICRO AND NANOTECHNOLOGY ENGENEERING

NOVA University Lisbon

October 2024

DEPARTAMENT OF
MATERIAL SCIENCES

Low-cost Smart Ink for Intelligent Packaging

Dissertation submitted in partial fulfillment of the requirements for the degree of Masters in Micro and Nanotechnologies Engineering

Francisco Silva Nunes Martins

BSc in Micro and Nanotechnologies Engineering

Adviser: Suman Nandy
Principal Investigator, Cenimat-i3N, FCT-NOVA

Co-advisers: Santanu Jana
Auxiliary Researcher, Cenimat-i3N, FCT-NOVA

Examination Committee:

Chair: Pedro Miguel Cândido Barquinha,
Associate Professor, FCT-NOVA

Rapporteurs: Daniela da Silva Nunes Gomes,
Assistant Professor, FCT-NOVA

Adviser: Suman Nandy,
Principal Investigator, Cenimat-i3N, FCT-NOVA

MASTER IN MICRO AND NANOTECHNOLOGY ENGENEERING

NOVA University Lisbon
October 2024

Low-cost Smart Ink for Intelligent Packaging

ACKNOWLEDGMENTS

The conclusion of this master's thesis represents a pivotal moment in my academic and personal journey, reflecting the culmination of numerous challenges and hardships, but also moments of triumph and personal growth. Throughout this journey, I have been fortunate to be surrounded by an incredible group of people who made the past years memorable, contributing to experiences that I will carry with me forever, and were essential in shaping my academic growth. It is with heartfelt gratitude that I acknowledge their support and presence.

I would like to start by extending my gratitude to Professor Elvira Fortunato and Professor Rodrigo Martins, which spearheaded the advancements of nanotechnology in Portugal, implementing the means for the creation of the course i am now graduating from, and that has been a central part of my life for the past five years. Thank you to Principal Investigator Suman Nandy, Auxiliary Researcher Santanu Jana, and researcher Sumita Goswami, for the support, advice, and guidance throughout this research. Without their contributions, the work presented here would not have been possible. Moreover, a very special thanks to PhD students Guilherme Ferreira and Rafael Resende, who went above and beyond in helping me to complete this project, providing not only excellent advice and fresh perspectives but also essential motivation and guidance. I would also like to express my appreciation for the immense list of people in CENIMAT and CEMOP, who were always attentive, supportive and a reference both in academic and personal aspects. This work was financed by national funds from FCT - Fundação para a Ciência e a Tecnologia, I.P., in the scope of the projects LA/P/0037/2020, UIDP/50025/2020 and UIDB/50025/2020 of the Associate Laboratory Institute of Nanostructures, Nanomodelling and Nanofabrication – i3N)- Also the work was partially developed under the project BRIGHT (Project reference: M-ERA-NET3/0004/2021) and From Fossil to Forest (PRR).

There are not enough words to express my gratitude towards my family and friends….Nevertheless, I would like to extend my most profound and heartfelt thanks to my mother and father for the values, knowledge, and beliefs they have instilled in me, which have had a monumental impact on who I am today and who I will become. I am deeply thankful not only for their unwavering celebration of my achievements but, even more so, for their support during the more challenging moments of my life. To my family as a whole, your encouragement and collective belief in me has fueled my determination and inspired me to pursue my goals with passion and resilience, for which I am forever thankful. As for my friends, each of you made me better as a person and provided me with wisdom, comfort, and incredible moments that allowed me to become someone of which I am truly proud. I cherish the countless memories we have shared, and I look forward to creating many more in the future.

“All truths are easy to understand once they are discovered;
the point is to discover them.” (Galileo).

ABSTRACT

The evolution in packaging industry has led to the development of intelligent packing solutions, which demands the incorporation of intelligent sensors and antennas into the packaging materials. Such changes allow to better ensure the safety and quality of perishable goods, through control of a multitude of parameters, including humidity, temperature and/or chemical changes. The development of functional and accurate intelligent packaging elements will allow to reduce illnesses caused by the consumption of expired or unsafe products, the negative economic impact that waste has in the supply chain, and the unnecessary pressure it creates in different limited natural resources. Given the need for further development around the topic, the aim of this research was to optimize the composition, production, and patterning of Ti_3C_2 (MXene)-based functional ink on paper substrates, for the production of eco-friendly, low-cost, and flexible paper-based antennas and humidity sensors. The choice of material was based on the unique properties of MXene, well suited for this work, including its high surface to volume ratio, exceptional conductivity, great stability, and hydrophilic characteristics, attributed to surface functional groups formed during solution processing stages. By patterning a paper substrate with conductive MXene ink it was possible to produce self-powered circuitry design when paired with a polydimethylsiloxane sheet, for which the output dependency on force and frequency of impact was evaluated. Under an applied force of 20 N at 2 Hz the maximum power density and current density obtained was 0.26 W/m^2 and 16.89 mA/m^2, respectively. This energy harvesting potential was used as input for different antenna designs, within which the best performing one presented a 3.75% efficiency. Additionally, humidity sensing capabilities of MXene were analyzed, for a relative humidity range of 10-60%, by evaluating changes on the electrical impedance of the device.

Keywords: MXene, Paper Electronics, Intelligent Packaging, Humidity Sensor, Circuitry designs.

RESUMO

A evolução da indústria de embalagens levou ao desenvolvimento de soluções de embalagem inteligentes, o que exige a incorporação de sensores e antenas inteligentes. Estas alterações permitem garantir a segurança e a qualidade dos produtos perecíveis, através do controlo de uma multiplicidade de parâmetros, incluindo níveis humidade, condições de temperatura e/ou alterações químicas. Progressos relacionados com a funcionalidade e precisão destes dispositivos, permitirá reduzir as doenças causadas pelo consumo de produtos fora de prazo ou inseguros, o impacto económico que o desperdício tem na cadeia de abastecimento e a pressão desnecessária que cria sobre diferentes recursos naturais limitados. Dada a necessidade de um maior desenvolvimento em torno do tema, o objetivo desta investigação foi otimizar a composição, a produção e a padronização de amostras de tinta funcional à base de Ti_3C_2 (MXene) em substratos de papel, permitindo a produção de antenas e sensores de humidade ecológicos, de baixo custo e flexíveis, à base de papel. A escolha do material baseou-se nas propriedades únicas do MXene, adequadas a este trabalho, incluindo a sua elevada relação superfície/volume, excecional condutividade, boa estabilidade e características hidrofílicas, atribuídas aos grupos funcionais de superfície formados durante as fases de processamento da solução. Através da padronização de substratos de papel com a tinta condutora de MXene e combinando estas estruturas com polidimetilsiloxano, foi possível conceber nano geradores triboelétricos, para os quais foi avaliada a dependência do sinal produzido em relação à força e à frequência do impacto a que os dispositivos foram submetidos. Sob uma força aplicada de 20 N a 2 Hz, a densidade de potência máxima e a densidade de corrente máxima obtidas foram de 0,26 W/m² e 16,89 mA/m², respetivamente. Esta capacidade de conversão de energia mecânica em energia elétrica foi utilizada para produzir o sinal de entrada para diferentes antenas, para as quais o melhor desempenho registado correspondeu a uma eficiência de 3,75%. Além disso, a possível utilização do Mxene para a deteção de níveis de humidade foi analisada, para uma gama de humidade relativa de 10-60%, através da avaliação das alterações na resistência elétrica do dispositivo à medida que as condições de humidade variavam.

Palavras-chave: MXene, Eletrónica em Papel, Embalagens Inteligentes, Sensores de Humidade, Projeção de Circuitos.

CONTENTS

LIST OF FIGURES

LIST OF TABLES

ACRONYMS

CA	Contact Angle
CAGR	Compound Annual Growth Rate
DI	Deionized Water
e-waste	Electronic Waste
IoT	Internet of Things
LED	Light Emitting Diode
RF	Radio Frequency
RFID	Radio Frequency Identification Device
RH	Relative Humidity
SC	Supercapacitor
SDG	Sustainable Development Goal
TENG	Triboelectric Nanogenerator
TMD	Transitional Metal Dichalcogenides
TMO	Transitional Metal Oxide
USD	United States Dollars
WSN	Wireless Sensor Networks

SYMBOLS

$\boldsymbol{\theta}$	Angle
$\boldsymbol{I}$	Current
$\boldsymbol{\beta}$	Full Width at Half Maximum
$\boldsymbol{d}$	Interplanar Spacing
$\boldsymbol{I_{MAX}}$	Maximum Current Density
$\boldsymbol{P_{MAX}}$	Maximum Power Density
$\boldsymbol{V_{OC}}$	Open-circuit Voltage
$\boldsymbol{n}$	Order of Diffraction
$\boldsymbol{P}$	Power
$\boldsymbol{R}$	Resistance
$\boldsymbol{K}$	Scherrer constant
$\boldsymbol{I_{SC}}$	Short-Circuit Current
$\boldsymbol{V}$	Voltage
$\boldsymbol{\lambda}$	Wavelength

1

INTRODUCTION

1.1 Context and Motivation

The packaging industry is developing at a rapid pace, with one of the most impactful technological changes being related to the attempt to incorporate intelligent packaging solutions. The integration of intelligent packaging allows to better ensure the safety and quality of perishable goods, through rigorous control of a multitude of parameters, including pressure, humidity, temperature and/or chemical changes [1], [2]. In the basis of these capabilities are a set of indicators and sensors paired with antennas and data carriers which allow to rapidly acquire, store and transmit data during transport and storage stages [3]. The development of functional and accurate intelligent packaging elements will allow to reduce illnesses caused by the consumption of expired or unsafe products, the negative economic impact that waste has in the supply chain, and the unnecessary pressure it creates in different limited natural resources [1].

These developments in the packaging industry also coincide with the upbringing of Industry 4.0, focused on digitization and automation of the industrial processes through the implementation of sensors and antennas [4]. Part of the industrial process corresponds to the control during storage and transport stages, made possible by the mentioned intelligent sensors and antennas incorporated into the packaging materials. In order to produce these devices at large volumes and at low-cost, printed electronics are expected to take on a central role [5]. This route also helps to address concerns related with sustainable technological development and usage of existing resources, reducing the pressure set on raw materials and the environment, partially mitigating the impact of electronic waste [6], [7]. The paper-based electronics sector has been the focus of extensive research, due to its lightweight, low-cost, and environmentally-friendly characteristics. The most diverse electronic components and devices have been developed, including nanogenerators, antennas, sensors, transistors, and supercapacitors [8]. Although satisfying results have been presented in this area, there is still a gap in knowledge related with new upcoming materials and their possible usage, which can lead to more stable, durable, rapid responding devices in comparison with the ones that exist, as well as, new untapped applications.

For such reasons, the aim in this research was to optimize the composition, production, and patterning of Ti_3C_2 (MXene)-based functional ink on paper substrates, taking the first steps towards the production of sensitive, eco-friendly, low-cost, flexible paper-based antennas and paper-based humidity sensors, which can be adapted in the future to incorporate intelligent packaging solutions.

By combining the 2D structure surface properties, the high conductivity and great stability from the MXene functional ink , with a paper based substrate, it was possible to produce a self-powered circuit, that provided the input for a set of different antenna designs for which the input-output relationship of the

transmitter/receptor structures were analyzed. Furthermore, the produced MXene functional ink also presents great hydrophilicity due to the presence of hydroxyl and fluorine groups [9]. As such, by combining a paper based substrate with conductive silver ink electrodes printed on the surface, with deposited layers of this functional ink, it was possible to develop a humidity sensing device. The humidity sensing capabilities of this device were tested in the relative humidity range of 10% to 60%. Therefore, this research will help to address different matters, including the need for research on the fairly new and unexplored 2D material that is MXene, while also attempting to make advances in intelligent paper-based humidity sensors and antennas, which represent the backbone of the current 4th Industrial Revolution, highly present in the packaging industries. As mentioned in this sector data acquisition and transmission is fundamental to ensure the integrity of perishable goods during storage or transport stages. Concerns surrounding sustainable technological development were also considered, with the aim to also contribute towards technological innovation at industrial level (SDG #9), and eventually help towards the construction of sustainable cities and communities (SDG #11) [10].

1.2 Research Background

1.2.1 A Packaging Industry Overview: Role of Paper

The employment of paper or cellulose-based substrates has already been explored in a wide range of electronic components and devices, including transistors [11], nanogenerators [12], supercapacitors (SCs) [13], light-emitting diodes (LEDs) [14], and sensors [9], [15], which have consistently showed progress in terms of accuracy, response time, stability, and long-term durability. One of the main reasons behind this vast development related to paper-based electronics, in particular sensors, is based on the unique advantages it offers, when compared to other substrates like metal, polymers or glass, which show challenges related with their heavyweight, oxidation, cost, or affinity [16]. These cellulose-based substrates are light weight, eco-sustainable, renewable, and highly available, presenting themselves as a great choice for the production of multiple devices [16].

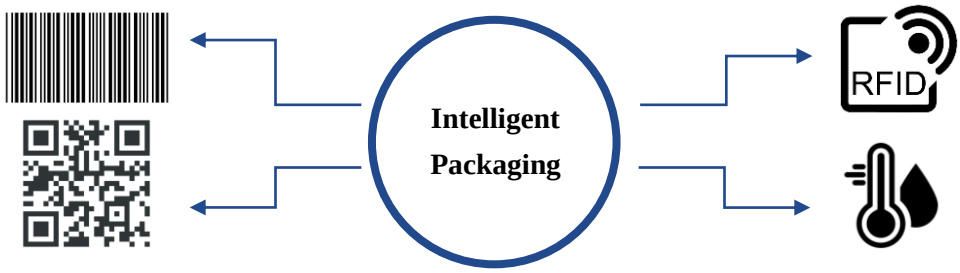

Figure 1.2.1.1 — Intelligent Packaging Solutions: Examples of devices utilized in the intelligent packaging sector for identification and quality monitoring of perishable goods, including code bars, QR codes, RFID transmitters and humidity/temperature sensors.

In the intelligent packaging sector, the main focus is on tracking and authentication devices, such as barcodes and QR codes, combined with quality monitoring sensors and indicators for effective product quality control [1]. This revolution in the packaging industry is parallel to the great evolution that all industries are undergoing, associated with Industry 4.0. Recent developments have been leading towards complete digitization and automation of industrial processes, ensuring the highest efficiency, deeming necessary the implementation of new technologies and control methods [4]. Consequently, with the proliferation of Internet of Things (IoT) associated devices as part of this Industry 4.0, the demand for intelligent devices in the fields of packaging, textiles, medical/health-monitoring, and many others, tends to drastically increase. To meet these requirements, is expected that printed electronics will take on a central role in the current and upcoming world of

interconnected devices, sensors, and services, allowing for the manufacturing of flexible circuits in large volumes and at low costs, with a great variety of applications [5].

Considering the previous points, not only has there been a great interest surrounding the possibilities of printed electronics, but there is also a need to achieve new and greater plateaus in terms of functionality and production capacity. This eminent growth is accompanied by radical changes in printed electronics market size, which can be forecasted. As of 2024, the global printed electronics market was valued at over USD 16 billion, and with current world changes the forecast is to reach close to USD 84 billion by 2034. This growth represents a compound annual growth rate (CAGR) of 17.42% during the period of 2024 to 2034 [17]. Although the majority of this market share is associated with the Asia Pacific region, which includes countries such as China, Japan, South Korea, and Australia, all key contributors towards the printed electronics market expansion, but it is significantly fragmented worldwide [17]. Taking all factors into consideration, it becomes clear that the current and especially the future role of printed electronics cannot be ignored. Continuous progress on current devices performance and innovative applications are needed and must be incentivized. This research is intended to extend the reach of paper-based electronics, through the employment of the upcoming 2D material, MXene.

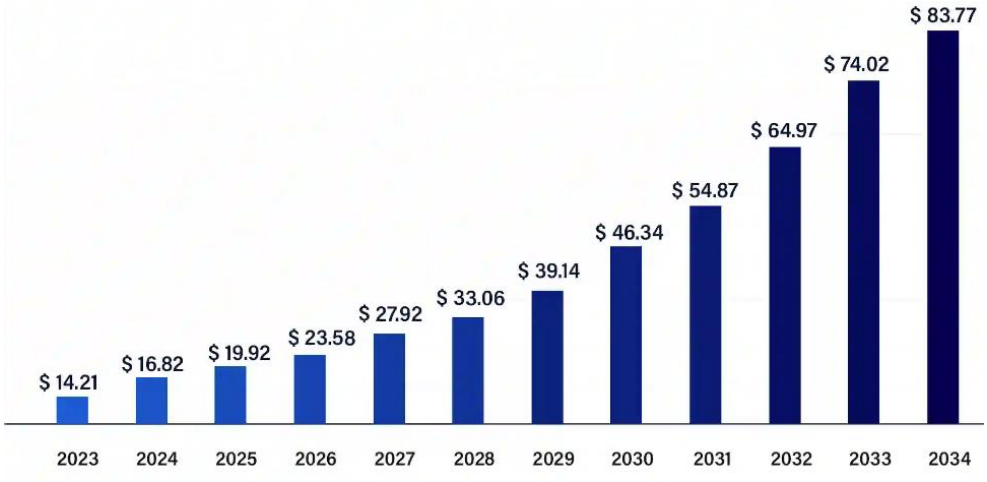

Figure 1.2.1.2 — Printed Electronics Market Size from 2023 to 2034 (USD Billion). Adapted from [17].

1.2.2 MXene Materials: Properties and Applications

So far, a large number of nanomaterials have been synthesized and used as sensing components for various applications, including strain/stress, gas, humidity and more. Among all the candidates, 2D materials have excellent material properties for sensor applications due to their large surface to volume ratio and unique electrical, mechanical, and optical properties [18].

Within the vast field of 2D materials, several candidates, including graphene, transition metal dichalcogenides (TMDs), graphitic carbon nitride, hexagonal boron nitride, and transition metal oxides (TMOs), have been explored and incorporated in diverse applications, attracting great attention, particularly in sensor related technologies [19]. Of all these different materials characteristics such as availability, toxicity, stability, and ease of synthesis must be considered. For the materials mentioned above, some or all of these properties do not meet the necessary requirements to be used in this project. Therefore, Ti_3C_2 (MXene) which possesses high conductivity, excellent flexibility, chemical stability, as well as outstanding mechanical robustness, represents the appropriate choice for the development of antenna structures. In addition, MXene has a large number of hydroxyl (-OH), and fluorine (-F) groups formed during the etching process, hence, it has good hydrophilicity

[18], becoming particularly suitable for humidity sensing purposes. Both these applications, employing MXene, are still in the early stages of research, leading to an increased emphasis on research. Based on the performance results obtained in this research, adjustments and optimizations of the structures can facilitate the development of intelligent devices in future stages of production.

All of the properties associated with this considerably new 2D material, MXene [20], are correlated with its structure. The name corresponds to an abbreviation of the 2D transition metal carbide, nitride, and carbonitride family. It presents an intermediate layer "A", composed of aluminum (Al), silicon (Si), tin (Sn) or indium (In), which is etched from the MAX phase through the reaction with a mixture of lithium fluoride (LiF) and hydrochloric acid (HCl). From this process a layered MXene is obtained, with a molecular formula of $M_{n+1}X_nT_z$, where n = 1, 2, or 3, representing three common structures. The "M" represents a transition metal such as titanium (Ti), vanadium (V), chromium (Cr), or manganese (Mn), the "X" represents a carbon (C) or nitrogen (N) element, and the "T" is correlated with a surface group such as oxide groups (O_2^-), hydroxyl groups (OH^-), fluoride groups (F^-), amine groups (NH_2^-), or ammonium groups (NH_4^+). The presence of the suffix "ene" is to emphasize the existing similarity with graphene [21].

1.2.3 Current Advancements in Printed Paper Electronics

1.2.3.1 Self-powered Circuitry Design

The first publication related to triboelectric nanogenerators (TENG) was released back in 2012 [22]. Ever since, an increased interest in this form of nanogenerator structure has flourished, due to its capability to harvest ambient mechanical energy, and converting it into electrical energy through contact electrification and electrostatic induction phenomena [23]. Given the need for power supply solutions applied to small electronics including sensors and transmitter structures, for which the power requirement is reduced, but demand low-cost, light-weight and compact power sources, flexible self-powered designs have attracted great attention, in particular flexible TENG structures. Considering the multiple advantages previously mentioned associated with paper substrates, including sustainability, stretchability, and low cost, cellulose-based substrates have also been in the basis of many of the developments around these flexible TENG devices [16],[24].

There are many available routes to produce a working TENG device, with increasing levels of complexity, associated with increasing costs and production difficulty. In its simple form the TENG structure requires the presence of a triboelectric layer, made from a material set high on the triboelectric series, which acts as the charge generating layer, and a conductive electrode layer that allows for the collection of generated charges. Making use of MXene high conductivity, stability, and patterning compatibility, it was possible to deposit layers of MXene conductive ink on paper, topping the structure with a polydimethylsiloxane (PDMS) sheet, composing a functional paper-based TENG flexible device. In this case, the paper sample will act as substrate, conveying structural integrity and flexible properties to the structure, the deposited MXene layer will act as the conductive electrode, and the PDMS as the triboelectric layer. Through automated or human interaction, by promoting repeated contact and separation cycles between the PDMS and MXene layer, is possible to generate a voltage output. These voltage peaks will be employed as input for the produced antennas, attesting for input-output relationship of the transmitter/receptor structure.

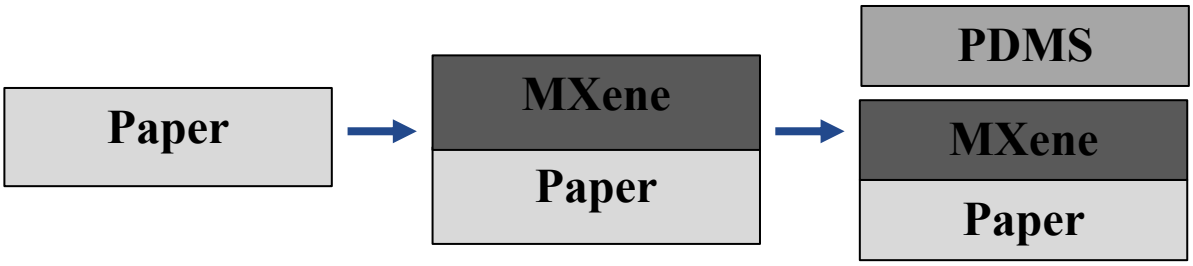

Figure 1.2.3.1.1 — TENG Production Schematic: MXene ink layers are patterned on top of the paper sample, and the PDMS sheet is placed of top of the structure.

1.2.3.2 Antenna Designs

Returning to the emergence of the IoT framework, the interconnection of the digital and physical worlds must happen through the usage of appropriate information and communication technologies without which IoT technology cannot exist or develop. Intelligent antennas represent the backbone of this sector, since it represents a critical component for sending and receiving information, to and from the processing tools of the IoT environment, in an adaptive and optimized manner [25]. Only this way the numerous devices interconnected in a given network can function and be operated at maximum efficiency. As such, flexible antennas with simple structures are becoming prominent in the communication sector, in particular related with the development of Radio Frequency Identification Device (RFID), and other wireless communication systems, such as Wireless Sensor Networks (WSN). These technologies are crucial for tracking, identification, automation, general data collection, and transmission, allowing for the implementation of IoT [26]. Furthermore, since the additive nature of printing techniques allows to reduce the volume of materials used and the waste created, partially mitigating the negative environmental impacts of the manufacturing process, while also being reliable in terms of scalability, cost-effectiveness, and high throughput, there has been a widespread adoption of the technology, particularly for printed RFID antennas [27].

Associated with the mass production of RF (Radio Frequency) electronics, with increased focus on performance paired with ease of production, design simplicity, reduced cost and light-weight structures, the communication antennas are usually printed using conductive ink. For the most part, copper, aluminum, and silver nanoparticle inks are the ones used for these applications. Although they show high-conducting properties, the metals integrated in these inks are rather expensive. Also, metals are not as suitable for sensing applications when compared to functional nanomaterials, so developing new strategies is of extreme importance, allowing for the eventual integration of sensing and communication capabilities in one device [28]. That is why, in this project a set of antenna designs were patterned on paper substrates, utilizing MXene functional ink, making use of its high conductivity and sensing adequacy. The input-output relationship of the transmitter/receptor structure was then attested for the different antenna designs. The performance of the device will depend on the conductivity of the ink, thickness, surface roughness, and the variations in the geometry of the designs.

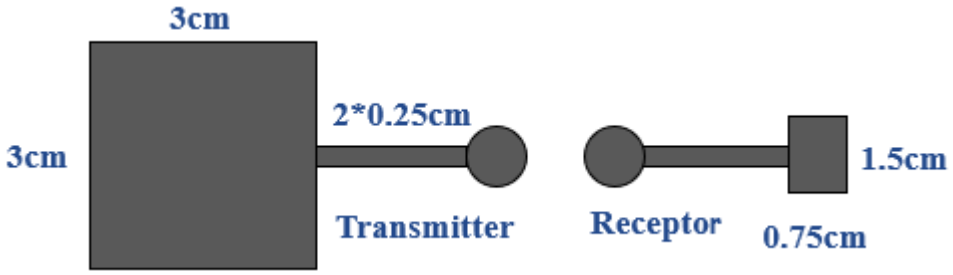

Figure 1.2.3.2.1 — Antenna Design Schematic: Schematic of Design 1, illustrating the general structure and the fixed parameters, consistent across all the designs.

1.2.3.3 Humidity Sensors

Humidity sensors find extensive applications in health, agriculture, and numerous packaging industries related to food, cosmetics, pharmaceuticals. Consequently, there is an increased interest and need related to devices capable of precisely monitoring relative humidity (RH) levels within wide operating ranges, with increased sensitivity, fast response and recovery times [29]. A great challenge is to determine how to produce such devices through a simple, cost-effective and environmentally friendly method. Within the different materials and structures analyzed, transition metal carbides and carbonitrides (MXene) have emerged as promising nanomaterials for humidity-sensitive applications due to their numerous hydrophilic active sites and reactive surfaces [18].

Bearing this in mind, the device analyzed in this research consists of a simple, low-cost, functional structure, which presents a resistive operative nature. On top of a paper substrate, an electrode structure was patterned through screen-printing, using silver ink. Layers of MXene ink were then deposited on top of this paper-electrode structure. This way the MXene sensing layer is exposed, promoting water adsorption due to its numerous hydrophilic active sites throughout its extensive surface area, which induces changes on the electrical impedance as a function RH (increasing or decreasing with changing levels of RH). Moreover, cellulose also presents great levels of hydrophilicity, which is beneficial for moisture adsorption. As such, this resistive humidity sensor presents adequate theoretical humidity sensitivity performance and good linearity [30][31].

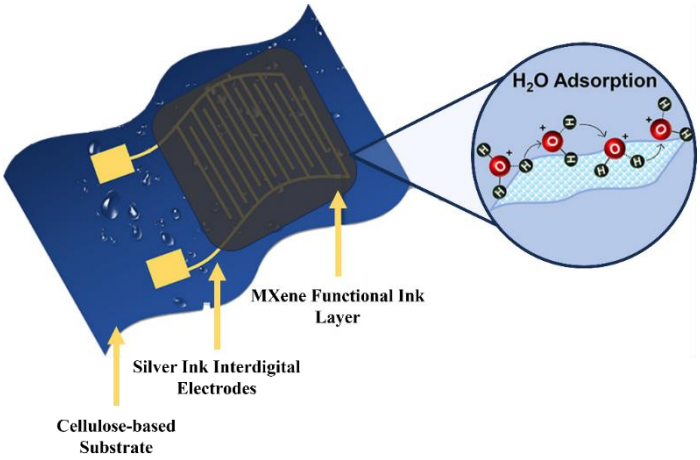

Figure 1.2.3.3.1 — Humidity Sensor Schematic: Proposed device composition and representation of the basic principle of operation. Adapted from [31]

As mentioned, owing to MXene surface chemical and physical properties, it exhibits significant potential for application in the field of humidity monitoring. However, limitations associated with reduced spatial structure density and the tendency to be oxidized in contact with more extreme environment conditions, which limits the hydration and dehydration of the structure, may affect the humidity sensing capabilities [32]. As such, extreme sensitivity levels, complete physical stability and oxidation resistance in a MXene-based humidity sensor remain a challenge and reveal the importance of continuous development surrounding the topic. Although, some of the mentioned problems present on pure MXene based devices have been reported to diminish when considering heterostructure (such as Ti_3C_2/TiO_2 sensing heterostructure) [29], the required processing increases total cost, time of production and overall device complexity. This way, there is still great interest and importance in attesting for the operation limits associated with purely MXene based devices, as once optimized these can show adequate performance for most required applications with reduced costs and greater simplicity.

2

MATERIALS AND METHODS

The MXene functional ink represents the base for the production of both the antennas, and humidity sensing device. The work carried out to achieve said devices was segmented in three major parts: the ink production from a MXene stock solution, the design, patterning, and evaluation of the input-output relationship of different antenna, and the design, production and performance analysis of the humidity sensor.

2.1 Ti_3C_2 (MXene) Ink Synthesis

For the production of conductive MXene stock solution, 2.4 g of LiF (Sigma-Aldrich) was dissolved in 22.5 mL of 9 M HCl solution (Merck), with continuous stirring for 30 minutes. After complete dissolution, 1 g of Ti_3AlC_2 powder was added to the previous solution, following stirring for 48 hours at 80ºC, with rotation set to 200 rpm, allowing to etch the Al element. After etching, the suspension was transferred to centrifuge tubes and washed several times with deionized (DI) water until the pH of the supernatant was around 6 (typically involved 6 washes). Each washing was carried by hand shaking and centrifuging at 3500 rpm for 5 minutes. The resulting suspension, still inside the centrifuge tubes, was sonicated for 1 hour, changing the water every 15 minutes to avoid increasing the process temperature, which should remain close to room temperature (close to 25ºC). At last, the centrifuge tubes were put back and centrifuged at 1500 rpm for 15 minutes. In this stage the precipitate was separated from the solution, which was carefully drained to a glass container and kept in the fridge at 4ºC. Following the production of the stock solution, in order to obtain the functional ink, 10 ml of said stock solution was allocated in a 50 ml flask. The ink was exposed to 120ºC for 4 hours under continuous stirring, set to 200 rpm. The produced ink was then labelled and kept in the fridge at 4ºC.

2.2 Self-Powered Circuitry Design

For the production of the TENG structure, a 3x3 cm square was designed through the Inkscape free software. The pattern was printed on office paper weighing 80 g/m^2 and placed inside the UV Ozone system, being exposed for 15 minutes without temperature. The first layer of MXene functional ink was then deposited, through the use of a paint pen (Pilot Parallel Pen), with a cartridge containing 1 ml of MXene ink. After deposition followed the curing process at 80ºC for 7 minutes. The same process was repeated for the second layer of MXene ink. For the third, and final MXene layer, the process was repeated, but for the curing process the exposure time increased to 12 minutes. As for the production of the PDMS sheet, 0.9 g of 184 silicone elastomer curing agent (Sylgard) were added to 9 g of 184 silicone elastomer base (Sylgard). The mixture was evenly spread on a square petri dish and exposed to 80ºC for 1 hour. Once the PDMS was solidified, 3x3 cm

samples were cut, and placed on top of the paper/MXene sample, following the performance analysis through mechanical impact.

2.3 Paper-based Printed Antenna

The desired antenna patterns were designed through the Inkscape free software. The different antenna designs incorporated changes in terms of transmitter/receptor area size combinations, while maintaining the distance from the center on the transmitter to the center of the receptor structure fixed at 1.5 cm, as well as the dimension of the remaining structures present on the design. The area of the transmitter/receptor varied between 0.5-2 cm^2, and all the possible combinations were attested. After printing the patterns silhouette, the substrates were prepared by the UV Ozone system. The patterns were exposed for 15 minutes without temperature. For the patterning of the MXene layers, the same process utilized during the TENG structure production was employed. Three total layers of MXene were deposited. The produced patterns were kept in the desiccator until testing.

2.4 Paper-based Humidity Sensor

After selecting the desired substrate (during the course of this investigation different substrates were employed, in particular office paper weighing 80 g/m^2, and Navigator™ raw paper substrates weighing 40 g/m^2, 80 g/m^2, and 100 g/m^2) six interdigital electrodes were patterned through screen-printing using silver ink (Saral SilverH2O 600) on a 5x7.5 cm sample. For the curing process, a hotplate was set to 60ºC, and the sample was dried for 6 minutes. From all the available patterns, the best one was selected and individualized. Following electrode deposition, three layers of MXene functional ink were deposited, through the previously discussed method. During the patterning of electrodes surface with the MXene ink, only the interdigitate portion of the electrode was covered, leaving the silver contacts at the end of the electrode structure exposed and intact for data acquisition during testing. All excess substrate surrounding the humidity sensing device was cut out. After production, the device samples were kept in the desiccator until testing.

2.5 Characterization Techniques

The structural, chemical, and optical analysis of the MXene stock solution were conducted through X-ray diffraction (Malvern PANalytical Aeris Benchtop X-Ray Diffraction System), FTIR Spectroscopy (Thermo-Scientific Nicolet Summit X FTIR Spectrometer), Raman spectroscopy (Renishaw InVia Raman Micorscope), and through UV-VIS-NIR spectroscopy (PerkinElmer Lambda 950 UV-VIS-NIR Spectrophotometer). The rheological properties of the different inks produced were determined through a rheometer (Anton Paar, Modular Compact Rheometer: MCR 502) and were complemented by contact angle measurements (Contact Angle System OCA 15plus). As for the mechano-electrical studies, these were performed by recurring to a standard oscilloscope (Tektronix TBS 2022), and a programmed Arduino board (Arduino Uno Rev3 (ATMega 328P)) associated to a force sensor which composed the machine press utilized for the mechanical impact essays. In terms of the humidity sensing measurements, an electromechanical and ambient test chamber was employed (Weisstchnik TensileEvent, Tensile Test–Climate Chamber) in order to control the humidity levels to which the devices were exposed, while the resistance changes were recorded through the use of Keysight oscilloscope (Keysight B2902B Oscilloscope).

3

RESULTS AND DISCUSSION

The prerogative in this research is to obtain functional, durable and low-cost paper-based antennas and humidity sensors, that with the right adaptations and optimizations can take on a central role in monitoring and data acquisition processes in the context of intelligent packaging. Since both devices are based on MXene functional ink, accessing the structural integrity, chemical stability and suitable deposition methods for the ink is imperative. After ink production, is necessary to ensure a complete and even distribution of this functional ink throughout the substrate, while maintaining certain properties such as high conductivity and adequate adhesion, achieving the best performance for the produced devices. All these parameters will be further analyzed in the upcoming sections.

3.1 MXene Functional Ink Production and Characterization

For the production of MXene different methods have been investigated in recent years, resulting in different physicochemical properties. For the purpose of this research a LiF-HCl based etching route, followed by a delamination process through sonification, was chosen. In this section, not only solution production will be addressed but also the processing strategies used to obtain the final ink employed in the devices production.

3.1.1 MXene Solution Production

In order to obtain MXenes it is required to selectively etch the "A" element from MAX phases, where the denominated "A" element typically represents aluminum (Al), while the "M" element continues to represent the same early transition metal and "X" either C or N element present in the MXenes, as discussed in the introduction section. Said etching process shows great challenge due to the strong metallic bonding that exists between M-A elements [33]. The existing reports related to the etching of Al from Ti_3AlC_2 MAX phase, are mostly focused on wet-chemical etching in hydrofluoric acid (HF), or HF-containing, or HF-forming etchants [33]. The process does not break the chemical bonds directly, but instead HF selectively reacts with the Al in the MAX phase producing aluminum fluoride (ALF_3), which is soluble in acid, thus facilitating its removal. Given the numerous concerns surrounding the use of highly concentrated HF solutions, routes based on *in-situ* formation of HF through the mixing of LiF and HCl have gained increased interest, allowing for a new high-yield, safer, and faster method for MXene synthesis [34]. Part of the reason why such method was employed in this research.

The chosen route was greatly, but not only, motivated by the hazardous nature of highly concentrated HF solution. The HF concentration employed during the etching phase of the process has a notorious impact on the MXene surface functionality. It has been shown that etching processes involving low HF concentration solutions lead to high-quality MXene flakes with reduced defects, such as pin-holes, while also impact the number of -OH, -O and -F terminations, tending to increase the -O and reducing the -F (higher O/F ratio) [35]. The changes in the O/F ratio can lead to increased hydrophilicity, a property of paramount importance considering the usage of the ink for the production of a humidity sensing device, hence it can increase sensibility and overall performance. As such, a 4 M of LiF powder to a 9 M HCl solution ratio was employed, allowing to obtain a diluted HF solution with a low concentration in between 2-3 wt.%. Through this process was possible to promote the delamination into nanosheets, upon solvent exchange, to be done at ease simply by ultrasound exposure [36].

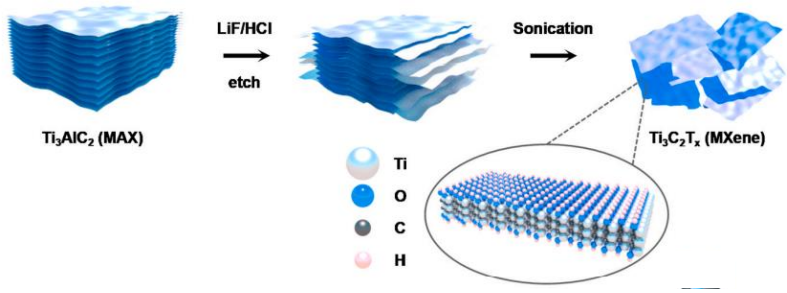

Figure 3.1.1.1 — Schematic Illustration of the Delaminated Monolayer MXene (Ti3C2Tx) Fabrication Process: Representation of both the etching and sonification phases of the process with additional atomic structure model in inset. Adapted from [36]

3.1.2 MXene Solution Characterization

3.1.2.1 Fourier-Transform Infrared (FTIR) spectroscopy

Theoretical suppositions related to the presence of -OH, -O and -F groups at MXene surface were confirmed through the FTIR spectroscopy. As a result of the etching process in LiF-HCl solution, we observe the presence of the typical FITR peaks at ~3310 cm^{-1} associated with -OH groups, at ~1623 cm^{-1} related to the stretching of C=O bonds, and at ~1074 cm^{-1} due to C-F bonds [37], [38].

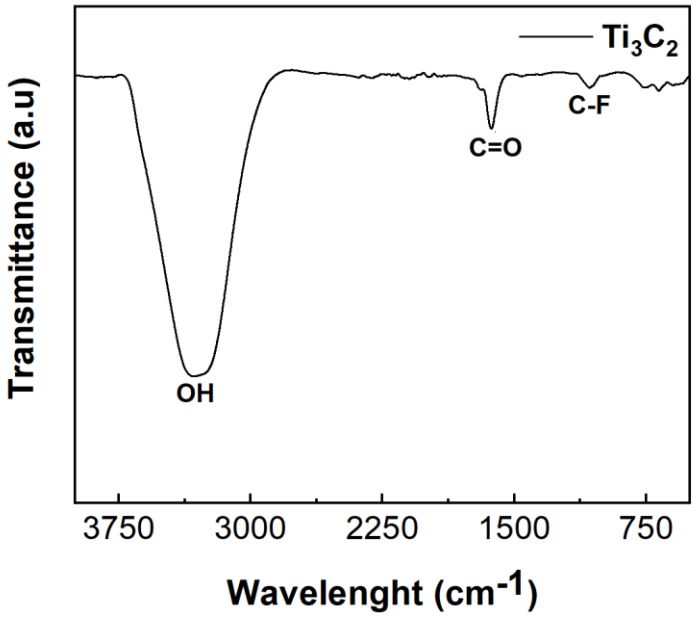

Figure 3.1.2.1.1 — Fourier-Transform Infrared (FTIR) Spectroscopy Spectra for the Produced MXene Solution.

The presence of -OH, -O and -F groups in the FTIR spectrum indicates the successful production of MXene solutions, as these functional groups are characteristic of properly etched and delaminated MXene flakes. Their formation is directly linked to the removal of aluminum from the MAX phase during etching, which introduces surface terminations critical for dispersion. These functional groups ensure the chemical stability and dispersibility of MXenes, enabling the formation of stable colloidal solutions necessary for various applications.

3.1.2.2 X-Ray Diffraction (XRD) spectroscopy

The FTIR analysis provided clear evidence of proper surface functionalization, indicating successful MXene production. In order to further support this conclusion, X-ray diffraction (XRD) analysis was also conducted. The results are presented in Figure 3.1.2.2.1, where the presence of a peak located at 2θ ≈ 6.2°, associated with the (002) plane, can be observed.

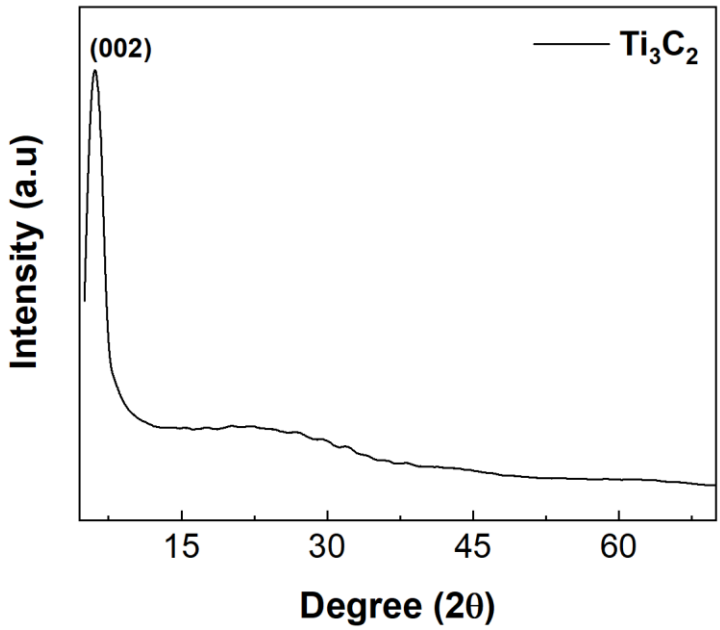

Figure 3.1.2.2.1 — X-Ray Diffraction (XRD) Patterns for the Produced MXene Solution.

The presence, position, and shape of the presented peak translates the different changes that occurred due to the LiF-HCl etching process, followed by sonification, of the MAX phase. When comparing the results obtained with literature, one of the clearest differences is the absence of the peak at 2θ ≈ 38°, associated with Al (104) plane, but also the change in position, and broadening, of the (002) plane peak which moves from values of 2θ ≈ 9.9° towards lower 2θ values, 2θ ≈ 6.2°, while visibly increases its full width at half maximum (FWHM) [39],[40]. These changes imply modifications both in d-spacing and "c" lattice parameters. Considering the Bragg law equation,

$$n\lambda = 2dSin(\theta) \qquad \textbf{(eq. 1)}$$

This decrease of the θ value, while maintaining the same order of diffraction (n) and wavelength of the X-rays (λ, corresponding in this case to 1.5418 Å due to the use of Cu Kα radiation), implies the increase of interplanar spacing, d-spacing. For the sample analyzed the interlayer spacing was calculated, and it was determined to be 14.26 Å.

Additionally, is important to consider that FWHM is inversely proportional to crystallite size, according with Scherrer equation,

$$\textbf{Crystallite size} \propto \frac{K\lambda}{\beta \cos(\theta)} \qquad \textbf{(eq. 2)}$$

Consequently, the broadening of the peak further indicated smaller nanoparticles on the HCl-LiF treated sample, what would be expected given the centrifugation and ultrasound exposure.

3.1.2.3 Raman Spectroscopy

Additionally, Raman spectroscopy analysis was also performed within the 540-1680 cm^{-1} wavenumber range. The results are presented in Figure 3.1.2.3.1. In accordance with literature, the peaks at ~630cm^{-1} and ~718cm^{-1}, are correlated with vibrations of the Ti-C bonds present in the Ti_3C_2 structure, in particular with out-of-plane and in-plane vibrations of the Ti and C atoms within each of the individual layers, respectively [41]. As for the peaks present at ~1293cm^{-1} and at ~1563cm^{-1}, these typically correspond to the characteristic D- and G-bands of carbon, related with sp^2 sites, present due to some free carbon and disorder in sample [41]. The reason why the disorder in the structure can be evaluated through the presence of these peaks is that G-band peak is correlated with the stretching of the C-C bond in carbon materials, while the D peak depends on sp^2 fraction and order and appears only if the sp^2 is in disordered rings [41].

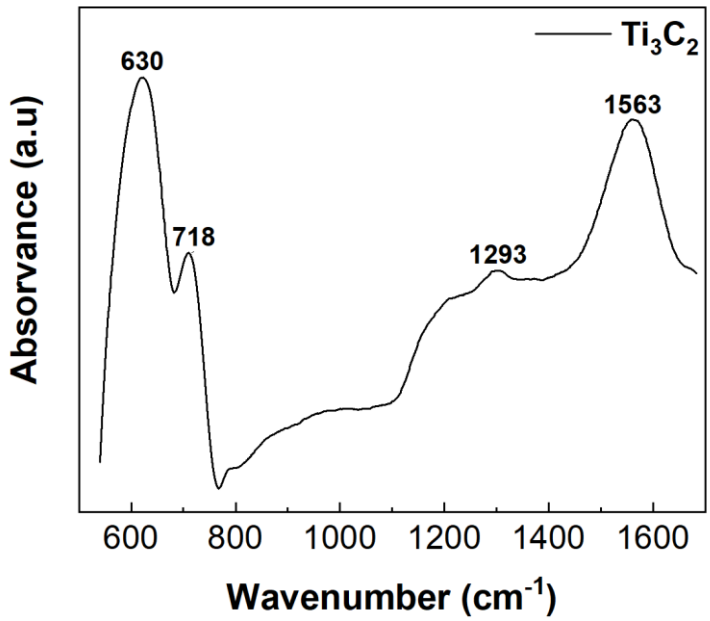

Figure 3.1.2.3.1 — Raman Spectra for the Produced MXene Solution.

3.1.2.4 UV-VIS-NIR spectroscopy

Furthermore, in Figure 3.1.2.4.1, it is possible to observe the UV-VIS-NIR Spectroscopy analysis results for an aqueous suspension of the produced MXene solution (0.04 mg/ml) for the 250-1000 nm range. It is worth noticing that the plasmonic properties of MXenes are intimately correlated with layer size, stacking properties, and functional terminations. In the UV-VIS-NIR spectrum, these plasmonic properties manifest as sharp absorption features, providing important information related with the structure properties. The presence of absorption peaks centered at ~253 nm and ~325 nm, as well as the one centered at ~762 nm, can be observed.

The presence of the peaks at ~253 nm and ~325 nm was expected due to surface functionalization of MXene with different groups after the etching of the A-element from its precursor ternary transition metal carbide (MAX phase). This absorption may correspond to the band-gap energy of the oxidized MXene, predicted through theoretical calculations. As for the ~762 nm peak, it is typically associated with the plasmonic properties occurring when free electrons on the MXene surface resonate with the incident light at this particular wavelength [42], [43].

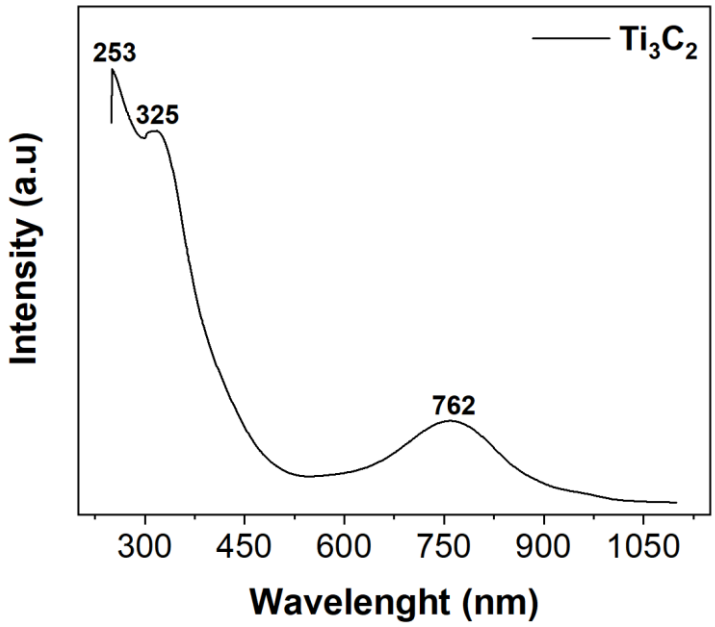

Figure 3.1.2.4.1 — UV-VIS-NIR Spectra for the Produced MXene Solution.

3.1.3 MXene Functional Ink Production

Through the production of the MXene solution we sought to achieve the necessary means for the patterning of highly-conductive layers of functional ink for the development of both the paper-based antenna and humidity sensing device, ideally through screen-printing. Due to its natural rheological properties, adjustments on solution viscosity had to be conducted, which was accomplished by promoting water evaporation.

Three distinct inks were produced, by considering three distinct evaporation times for MXene base solution samples, determining which ink was the most compatible for the research goals. For the designated "Ink 1" the evaporation time was 3.5 hours, for "Ink 2" the evaporation time was higher, at 4 hours, and for "Ink 3" the evaporation time was 4.5 hours. All the inks were produced at the same time, under the same environmental conditions, and a temperature of 120ºC, with stirring set to 250 rpm. This way was possible three different concentrations for each ink, which ended up being 35 mg/ml, 44 mg/ml and 54 mg/ml, for Ink 1, Ink 2, and Ink 3, respectively.

To evaluate which of the produced ink would be best for the task in hand, rheology tests were performed on all three inks, the results are presented below. In Figure 3.1.3.1 a), we can observe the shear thinning, or in other words pseudoplastic behavior, present in all inks, illustrated by the downward-sloping curve result of the viscosity decreasing with increasing shear rate values [44]. It is not surprising to see that for less viscous inks,

such as Ink 1, the viscosity significantly drops for lower shear rate values when compared with the remaining inks, due to reduced internal resistance to flow. Considering that this flow restrains result from the lack of particles aligned in the direction of flow, in combination with the particle network that forms in the suspension, as we move on towards higher concentrations will be harder to promote most particles on the sample to align in the direction of flow [44]. Such phenomena have great impact on wetting properties of the ink, and the significant drop of viscosity for lower shear rates from Ink 1 indicates better wetting properties, that progressively diminish as we move up towards Ink 3, shown by the increasing values of shear rate to promote equal viscosity drops.

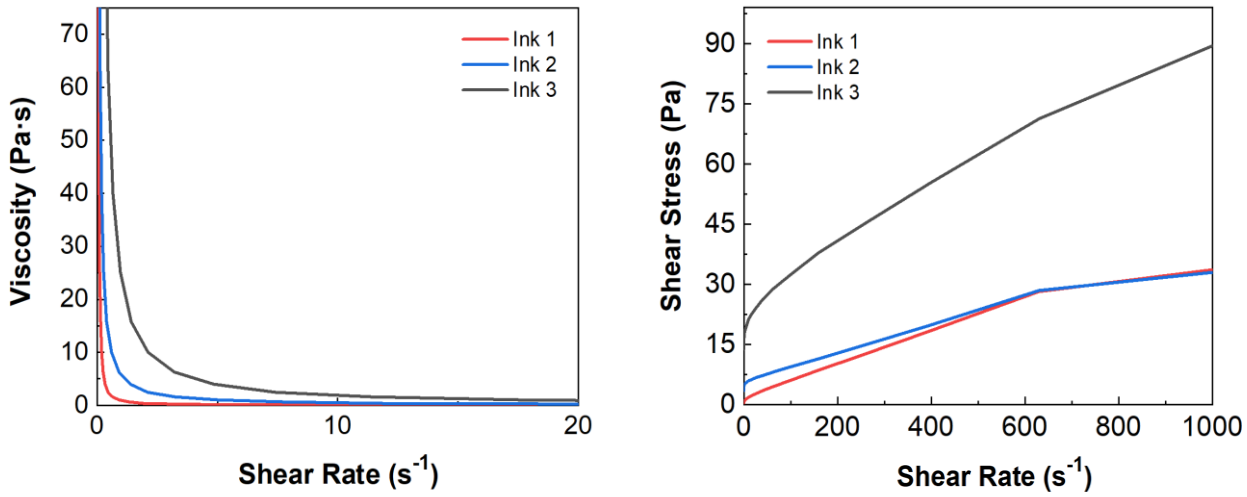

Figure 3.1.3.1 — Rheology Tests Results: (a) Viscosity *versus* Shear Rate results; (b) Shear Stress *versus* Shear rate results.

Furthermore, from Figure 3.1.3.1 b) the existence of yield stress for the tested inks is presented. As can be seen through the shear stress versus shear rate graph, none of the curves associated to each of the ink samples pass on the origin. This means that, they present a viscoelastic behavior, due to a given stress threshold, only after which they begin to flow [45]. Once again, this stress plateau is different considering the different viscosities of each ink, and resulting rheological properties, being higher for Ink 3, as it presents greater viscosity, and consequently greater flow resistance. It is important to notice that inks with lower yield stress values tend to be more suited for when a smooth and uniform coverage of surfaces is required since they provide a more efficient substrate wetting [45]. From the information obtained through this analysis, the most adequate inks for the devices production were set to be Ink 1 or Ink 2.

Following the rheological tests, contact angle essays were also performed, complementing the rheological information gathered and discussed before. Considering that during the course of this research, one of goals was to determine the impact of different paper-based substrates in terms of the humidity sensor performance, the contact angle measurements were performed in four different substrates which were later employed in the development of the proposed device. These paper substrates corresponded to regular office paper, weighing 80 g/m^2, and the remaining three corresponded to Navigator™ raw paper samples with three different weights, in particular 40 g/m^2, 80 g/m^2, and 100 g/m^2. In Figure 3.1.3.2 the results of the static contact angle measures are presented for all the mentioned substrates.

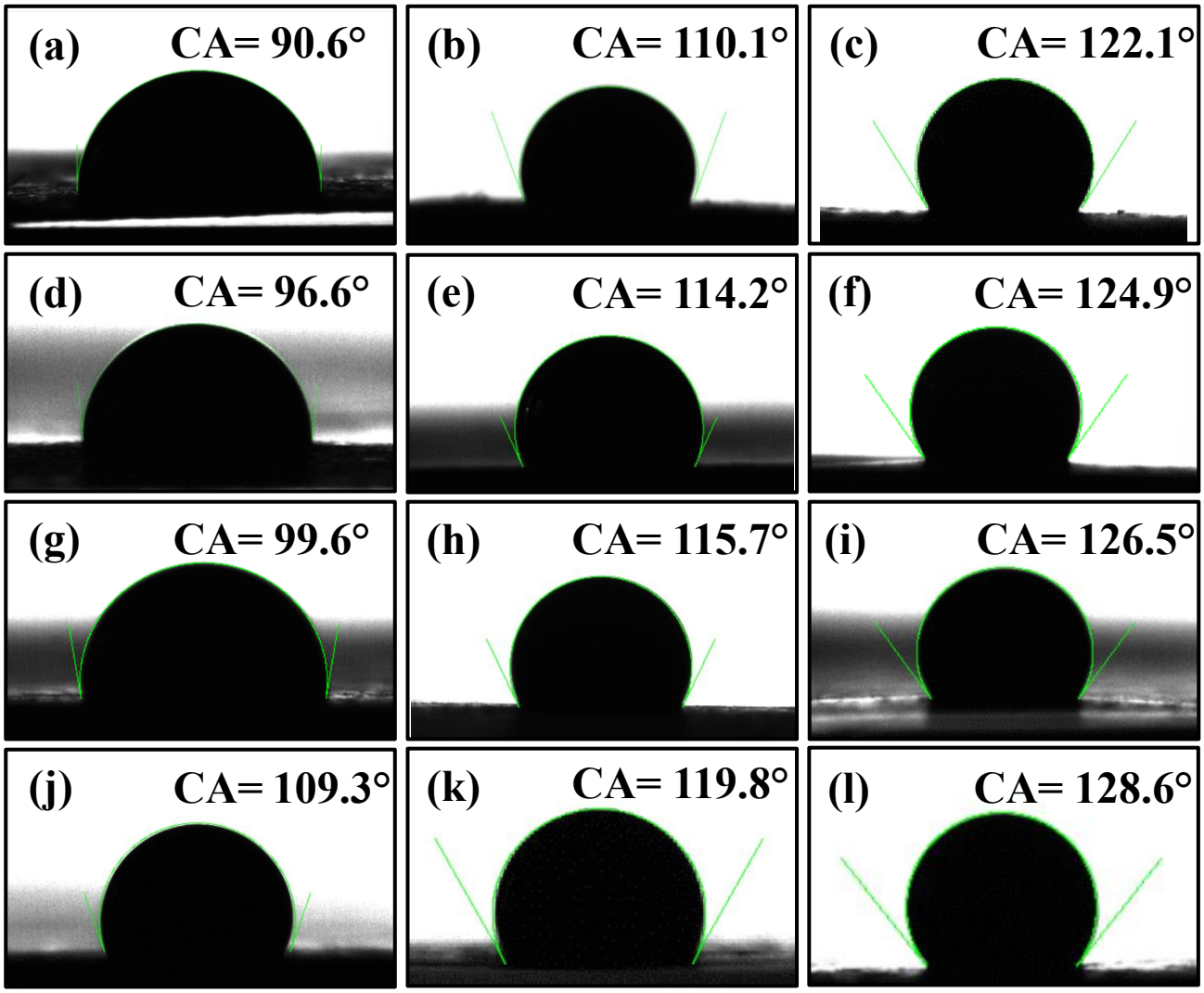

Figure 3.1.3.2 — Contact Angle Measurements: (a) Ink 1 on Navigator™ 40g/m^2; (b) Ink 2 on Navigator™ 40g/m^2; (c) Ink 3 on Navigator™ 40g/m^2, (d)) Ink 1 on Navigator™ 80g/m^2, (e) Ink 2 on Navigator™ 80g/m^2, (f) Ink 3 on Navigator™ 80g/m^2, (g) Ink 1 on Navigator™ 100g/m^2, (h) Ink 2 on Navigator™ 100g/m^2, (i) Ink 3 on Navigator™ 100g/m^2, (j) Ink 1 on Office paper; (k) Ink 2 on Office paper; (l) Ink 3 on Office paper.

Analyzing the different measurements, a considerable difference, related to the different wetting properties of the inks, can be observed. Both the ink utilized, and the substrate chosen show impact on the contact angle measurements, although the major differences are noticeable when switching between inks. For the Navigator™ 40 g/m^2 substrate, Ink 1 presented an average contact angle of 90.6±1.3°, while for Ink 2 and Ink 3 the average contact angle increased to 109.4 ±0.9° and 122.2 ±0.8°, respectively. As for the Navigator™ 80 g/m^2, the average contact angle for Ink 1, Ink 2, and Ink 3 corresponded to 96.5 ±0.8°, 114.3 ±0.7°, and 123.8 ±0.7°, respectively. While using the Navigator™ 80 g/m^2 substrate, the average contact angle increased, once again, to 100.4 ±1.1°, 114.9 ±0.6°, and 127.5 ±0.5°. When measuring the contact angle while using the office paper substrate, the average angle for all the three inks corresponded to 108.9 ±0.8°, 120.0 ±0.6°, and 127.6 ±0.5°.

Further supporting previous conclusions, moving from Ink 1 towards Ink 3, due to increase viscosity and changes in rheological properties, the wetting capabilities tend to diminish based on the increasing value of the contact angle associated with the ink droplet from each of the inks, on all the substrates analyzed.

An important aspect of this analysis was related to the impact of the substrates on ink deposition. Considering the different weights associated with the three Navigator™ raw paper substrates employed in this research, the 40 g/m^2, 80 g/m^2, and 100 g/m^2, different properties arise, both between each of the raw paper samples but also from the 80 g/m^2 office paper. It is important to notice that these raw paper substrates present minimal processing, reducing the physical and chemical treatments to which they are subjected to, when compared to the traditional office paper. This results in an unbleached and uncoated substrate that presents a rougher surface with higher exposure of the porous structure [46]. Consequently, if not coated, these substrates tend to present a higher absorption, with higher risk of ink spread, which will increase the difficulty when printing highly detailed, fine line structures though techniques such as screen printing, as for example closely spaced interdigitated electrodes structures [47]. These processing differences are certainly noticeable through the contact angle average values, which increase, indicating a diminishing wetting tendency, as the raw paper substrates weight increases up until the substrate changes to office paper.

Adding to the data acquired, the selection of the ink was made through empirical results. All three ink samples were attested for screen-printing. In Figure 3.1.3.3, we can see the results associated with the attempt to print an interdigitated electrode pattern on an office paper sample. Out of the three, Ink 2 clearly showed the best performance, allowing for a defined electrode patterning, with no unwanted conductive paths and in a uniform manner. As such, due to the performance seen from Ink 2 and all the previous information related to its rheological properties, this was the ink employed in the remaining of this research, which allowed to obtain smooth, uniform and highly conductive ink layers in the development of the different devices proposed. Given the mesh pattern limitations, during the course of this research alternative methods were also assessed. The main alternative was patterning the substrates by hand, through the use of an ink pen with the cartridge filled with MXene ink.

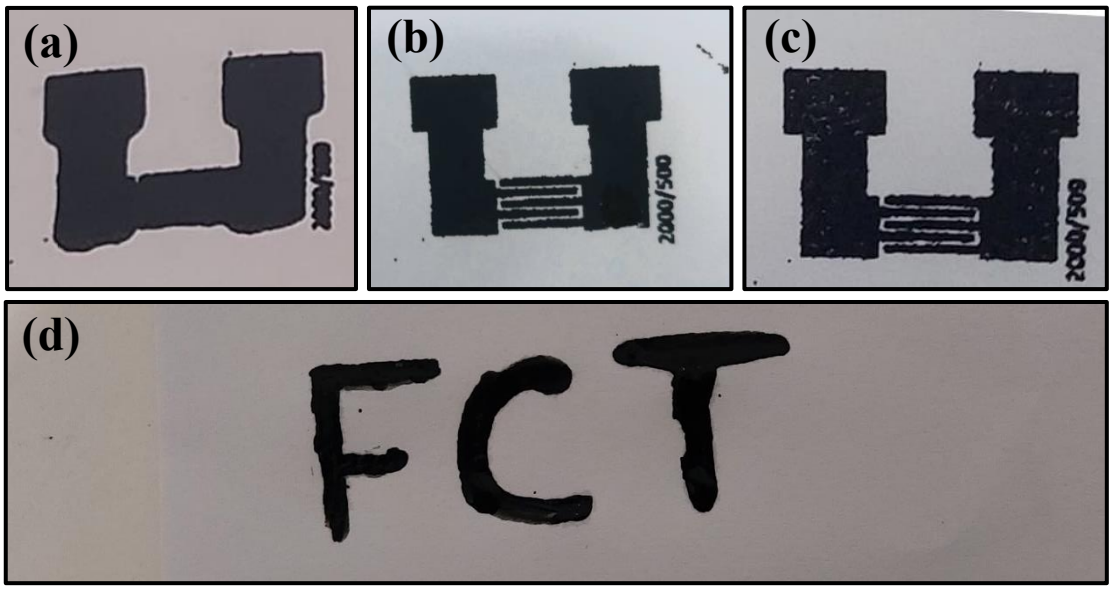

Figure 3.1.3.3 — Mxene Functional Ink Patterning Attempts: (a) Interdigitated electrode patterned with Ink 1; (b) Interdigitated electrode patterned with Ink 2 (c) Interdigitated electrode patterned with Ink 3, (d) Writing as a patterning attempt utilizing Pilot Parallel Pen filled with Ink 2.

3.2 MXene Self-powered Paper-based Circuit

Considering that one of the most prominent characteristics of 2D materials, including MXene, corresponds to their high conductivity, there was significant interest in utilizing this property for the production of paper-based circuitry. To harness this characteristic, a TENG structure was fabricated through the deposition of MXene ink on a paper sample, paring it with a PDMS sheet. In this structure the paper substrate and MXene ink layer provided the support substrate and conductive electrode respectively, while the PDMS provided the triboelectric layer required for a functional TENG structure. The charge generation was promoted through deformation of the PDMS layer, due to mechanical impact, and consequent triboelectric effect and electrostatic induction.

When pressure is exerted on the surface of the device, a contact electrification process occurs between the PDMS and the MXene layer. This phenomenon is mainly promoted by the difference in electron affinity between the two materials and an increase in effective contact area. Considering that PDMS is set lower in the triboelectric series, which means that is more electronegative when compared to MXene, this contact between layers results in the transfer of electrons from the MXene layer to the PDMS, causing a separation of charges, where the PDMS accumulates negative charges and the MXene layer accumulates positive charges. As for the release stage, a reverse electron flow is promoted, and the system resets with the charges being dissipated. These deformation and restoration cycles of the PDMS create dynamic changes in the contact area, leading to variations in the local electric field. These variations induce a potential difference, generating an electrical current when the circuit is closed. The produced current will depend on the value and velocity of the pressure that is applied, reason why the device output dependency on force and frequency will be attested for, as well as, current and power density [36].

As such, the process of pressing and releasing the PDMS layer converts mechanical energy into electrical energy, as the applied pressure drives the cyclic separation and recombination of charges. Consequently, this mechanism allows for continuous energy harvesting from mechanical stimuli, making it suitable for powering small devices or sensors in a self-sustained manner.

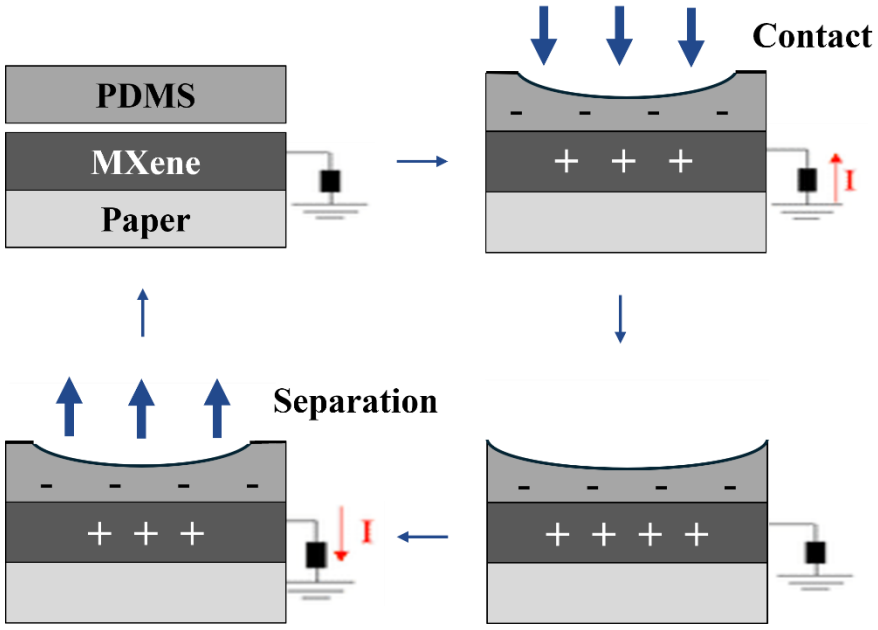

Figure 3.2.1 — **Proposed Working Mechanism Associated with the Flexible TENG Structure:** during periodic mechanical impact. Adapted from [36]

3.2.1 Device Patterning and Production

A major concern related to the device production is the quality of the pattern, ensuring full and dense coverage of the substrate, but also the durability of the structure. Only this way was possible to ensure reliable results and the best performance during measurements. During early stages of development multiple routes were pursued, in the attempt to achieve the best results in terms of pattern conformity, adherence, production time and resources required. These routes and associated results are presented in Figure 3.2.1.1. Considering there was not a screen-printing mesh with the required designs available, all the devices were manually patterned, either through a paint brush or ink pen, as discussed below.

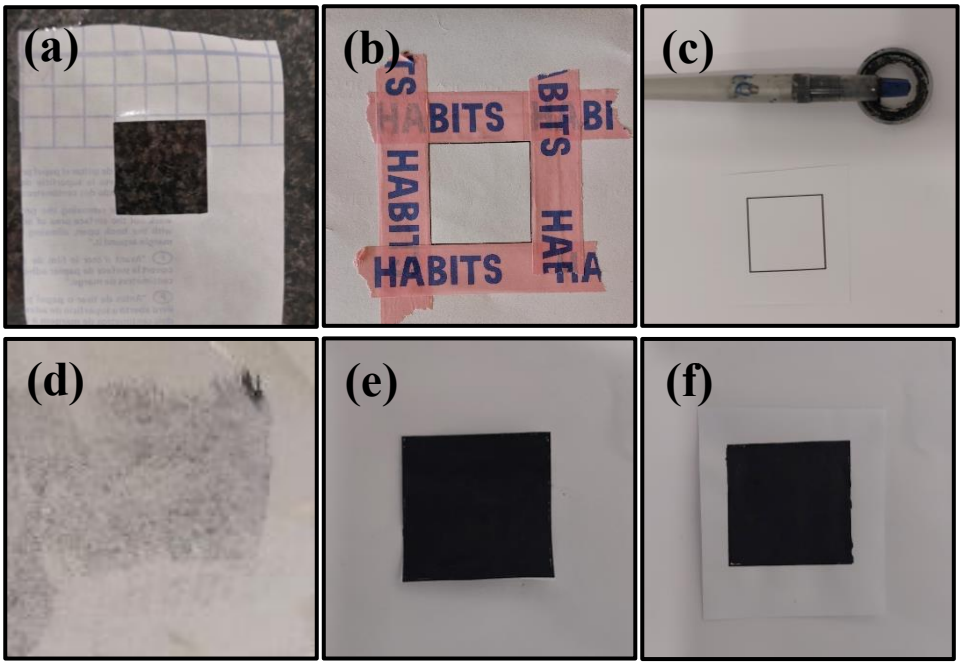

Figure 3.2.1.1 — TENG Structure Production Methods: (a) Contact paper mask; (b) Paper tape full contour; (c) Pilot parallel painting pen patterning, (d) Contact paper mask result, (e) Paper tape full contour result, (f) Pilot parallel painting pen patterning result.

In the first attempt, the proposed design was printed through the use of Cricut™ cutting machine onto a contact paper sample. This would allow for the production of a self-adhesion mask, which could be directly place on top of the chosen paper substrate and painted over, with the painting brush, transferring the square pattern. This route was time and resource effective, but due to the glue strength, heightened by the heat exposure during pattern drying stage, led to high substrate damage and pattern distortion due to ink being pulled during removal of the contact paper mask.

The last two methods presented the best results in terms of pattern conformity but presented significant differences. As presented in Figure 3.2.1.1 (b), for the second method the pattern was totally contoured using paper tape, and once again painted over with the paint brush. This method provided the means to attain good design conformity, and it allowed to produce structures with multiple ink layers with ease. The disadvantage relied on the increased production time, associated to the countering process of the design, when compared to the method presented in Figure 3.2.1.1 (c). In this last case, instead of employing a mask system and painting over with a paint brush, a paint pen was acquired and the cartridge filled with Mxene ink. This way it was possible to simply print the desired design shape and freehandedly paint the pattern. This method presented great improvements in terms of time, steps, and material required, while also further improving design conformity and ink adhesion.

3.2.2 TENG Structure Performance

3.2.2.1 Output voltage dependency on applied force

In the first stage of the device performance analysis, the open-circuit voltage (V_{OC}) output variation based on force applied was determined. From Figure 3.2.2.1.1 it is possible to observe the different outputs obtained through the impact at different forces, from 20 N up to 80 N, maintaining the impact frequency fixed at 2 Hz. As a consequence of increasing forces being applied, the output voltage value also increases.

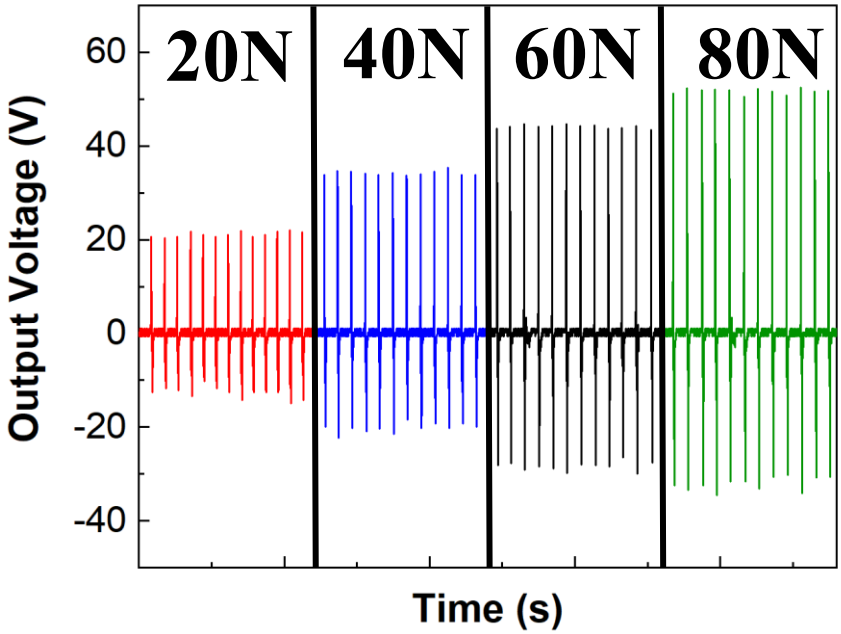

Figure 3.2.2.1.1 — Electrical Output Performance of TENG Structure: Open circuit voltage (V_{OC}) results as a function of different impact forces, including 20 N, 40 N, 60 N, and 80 N.

Beginning by analyzing the output obtained through the use of an impact force of 20 N, an average output voltage of 21.2 ± 0.5 V was registered. As the impact force increases to 40 N the average output voltage also increased to 34.0 ± 0.5 V. As we moved up towards 60 N, the output voltage value increased once again, to an average value of 44.0 ± 0.4 V. Finally, for the last force value tested, 80 N, the average output voltage value was determined to be 52.0 ± 0.5 V.

The output variation is due to the different degrees of deformation that different forces applied create on the surface of the PDMS layer. As a result of an increasing impact force, the PDMS and MXene layers are forced into greater proximity, increasing effective contact area and consequent charge transfer, which paired with the higher kinetic energy applied to the tribological layer, that provides higher degree of polarization, leads to overall higher charge generation and associated voltage output [48].

3.2.2.2 Output voltage dependency on applied frequency

Complementing the previous study, the influence of impact frequency was also assessed. For this essay, the impact force was set to 40 N, while the impact frequency increased from 1 Hz up to 3 Hz. As it can be observed from Figure 3.2.2.2.1, as the frequency increased, the V_{OC} output also increased.

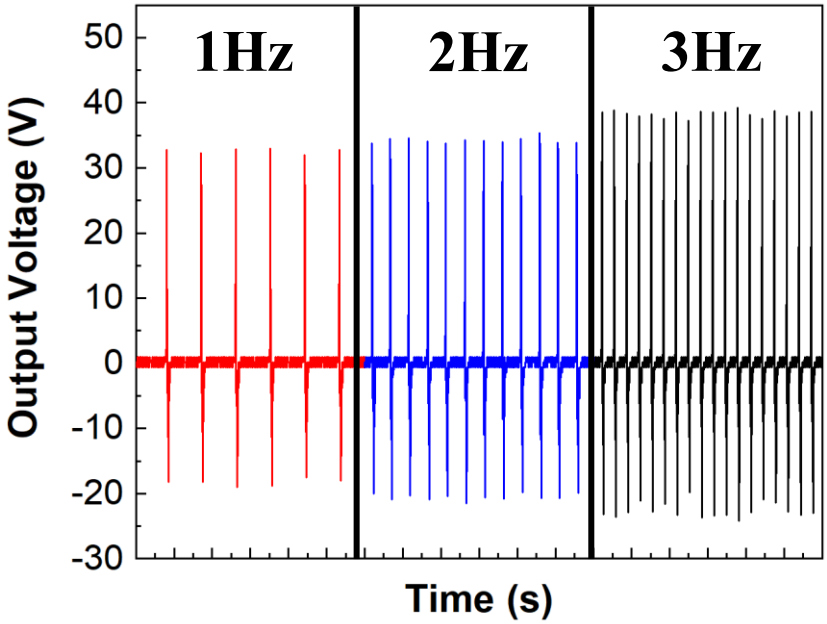

Figure 3.2.2.2.1 — Electrical Output Performance of TENG Structure: Open circuit voltage (V_{OC}) results as a function of different impact frequencies, including 1 Hz, 2 Hz , and 3 Hz.

For an impact frequency of 1 Hz, the average output voltage obtained was 32.6 ± 0.4 V. As the impact frequency changes to 2 Hz the average output voltage was, as presented before, 34.0 ± 0.5 V. As for the last case, utilizing an impact frequency of 3 Hz, the average output voltage value increased to 38.3 ± 0.5 V.

In this case, the changes in voltage output as a result of the increase in impact frequency arise due to different factors from the previous case. With increased impact frequency, deformation and release cycles become faster and more frequent leading to accumulated or residual charges that do not have time to dissipate in between cycles, slightly increasing the overall generated charges per cycle [48]. It can also be argued that with decreasing time between impact, phenomena like charge dissipation due to recombination are mitigated, which also tends to increase the output valuer per cycle.

3.2.2.3 Current and power output

Additionally, the short-circuit current (I_{sc}) as a function of a load resistance was evaluated, for an impact force of 20 N at 2 Hz. For such purpose the load resistance was varied from 250 KΩ to 75 MΩ, by progressively adding resistors connected in series on a motherboard, to each the device and oscilloscope were also connected. Through the measurement of the voltage at the ends of the connected resistors, while knowing the resistance value and area of the device, was possible to obtain the current and power density values.

It was observed that as the load resistance increased the current density decreased, proving that the TENG performance is dependent on the load resistance. A maximum current density (I_{MAX}) value of approximately 17 mA/m^2 was obtained with a load resistance of 1 MΩ. As for the maximum power density (P_{MAX}), it also peaked for a resistance value of 1 MΩ, attaining a maximum value of approximately 0.26 W/m^2.

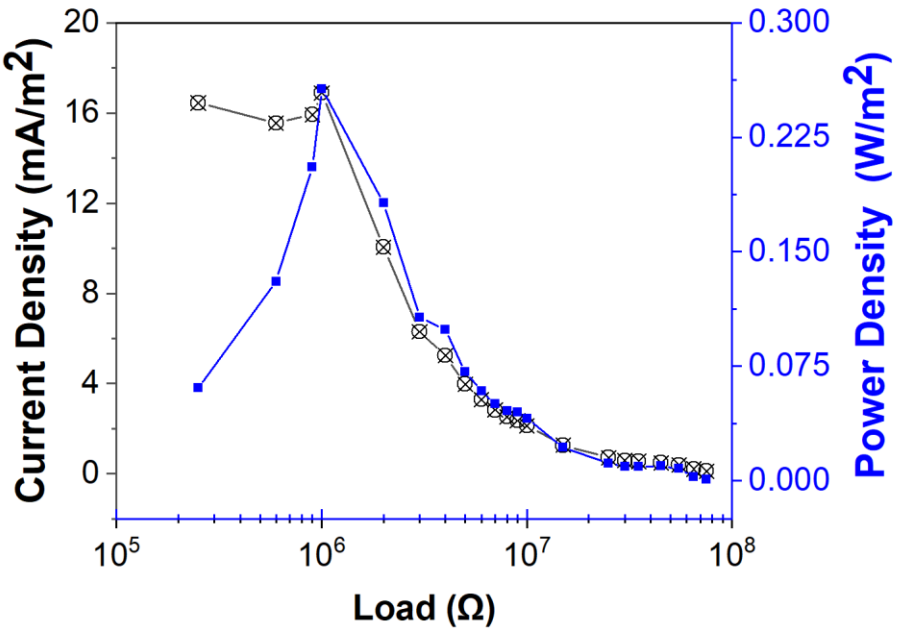

Figure 3.2.2.3.1 — Electrical Output Performance of TENG Structure: Current density and Power density results.

3.3 MXene Paper-based Antenna

In order to attest for the possible usage of MXene ink in the production of paper based antennas, different designs with varying sizes between transmitter and receptor structures were prepared. This way was possible to determine the impact of the transmitter/receptor size ratio in the antenna's performance. The different designs patterns are presented below, in Figure 3.3.1, and the specifications of these designs are summarized in Table 1.

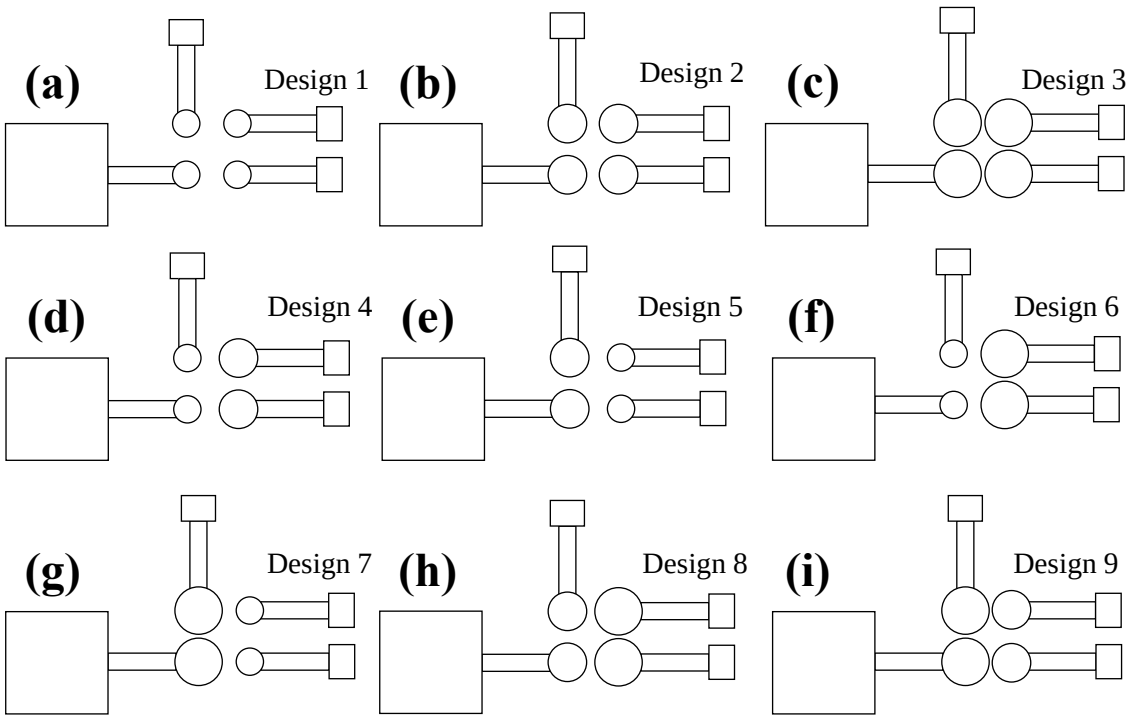

Figure 3.3.1 — Antenna Design Patterns: (a) Design 1, (b) Design 2, (c) Design 3, (d) Design 4, (e) Design 5, (f) Design 6, (g) Design 7, (h) Design 8, (i) Design 9.

Table 1 - Antenna Design Parameters by Design Number

Design Number	Transmitter Area (cm^2)	Receptor Area (cm^2)	Transmitter/Receptor Distance (cm)*
1	0.5	0.5	1.5
2	1.0	1.0	1.5
3	1.5	1.5	1.5
4	0.5	1.0	1.5
5	1.0	0.5	1.5
6	0.5	1.5	1.5
7	1.5	0.5	1.5
8	1.0	1.5	1.5
9	1.5	1	1.5

***Note:** The Transmitter/Receptor distance is related to the center to center distance.

3.3.1 Antenna Performance

The performance of antennas, including these circular patch antennas, is dependent on geometry, substrate properties, and feed mechanisms. Changes in any of these parameters will affect the resonance frequency, bandwidth, and gain of the antenna structure [49]. For this research, since the goal was to investigate the potential of MXene functional ink in the production of low-cost paper-based antennas, changes on the substrate were not considered, excluding efficiency tailoring though change of the substrate dielectric constant. The feeding mechanism also remained constant, as the input for the antenna's efficiency study was always based on the MXene/PDMS triboelectric effect. Nevertheless, changes in the transmitter and receptor circular structures were considered, while the remaining antenna structure remained identical throughout the different designs. Previous to the testing stage, the data related to the thickness and conductivity associated with each sample was collected. The results are presented below in Table 2.

Table 2 - Antenna Design Thickness and Resistance

Design Number	Thickness (μm)*	Resistance (Ω)**
1	116 ±0.5	7.1±1.5
2	119 ±0.5	10.7 ±2.6
3	117 ±0.5	8.2 ±0.7
4	116 ±0.5	9.1 ±1.5
5	118 ±0.5	6.3 ±2.2
6	114 ±0.5	9.7 ±1.8
7	116 ±0.5	9.9 ±2.1
8	121 ±0.5	9.5 ±1.0
9	117 ±0.5	8.3 ±1.3

***Note:** The thickness was measured through the use of a digital micrometer. ** The resistance was measured utilizing a multimeter, spacing the test probes 1 cm apart.

The performance of the different antennas designs was determined through the measurement of their efficiency. In order to obtain this data, the ratio between the input signal from the transmitter and the intensity of the output signal in the receptor was calculated. This input signal was obtained by utilizing a sheet of PDMS, measuring 3x3 cm, placed in the input section of the transmitter structure, also measuring 3x3 cm, making use of the MXene/PDMS triboelectric behavior attested previously. For the measurement of the input and output peaks, an oscilloscope was utilized. By connecting the first channel to the transmitter and the second channel to the receptor, both the input and output signals were quantified, allowing to proceed with the ratio calculations. An example of this analysis is presented based on the results obtained from the best-performing design, Design 3.

$$\textbf{Efficiency}\ (\%) = \frac{\textit{Output Voltage at Receptor}}{\textit{Input Voltage at Transmitter}} * \mathbf{100} = \frac{\mathbf{1.52}}{\mathbf{37}} * \mathbf{100} = \mathbf{4.05}\ \% \qquad (\mathbf{eq.3})$$

By repeating this analysis and calculation for all the recorded peaks, an average value can be obtained. Those average values were presented as the efficiency results for the design in question.

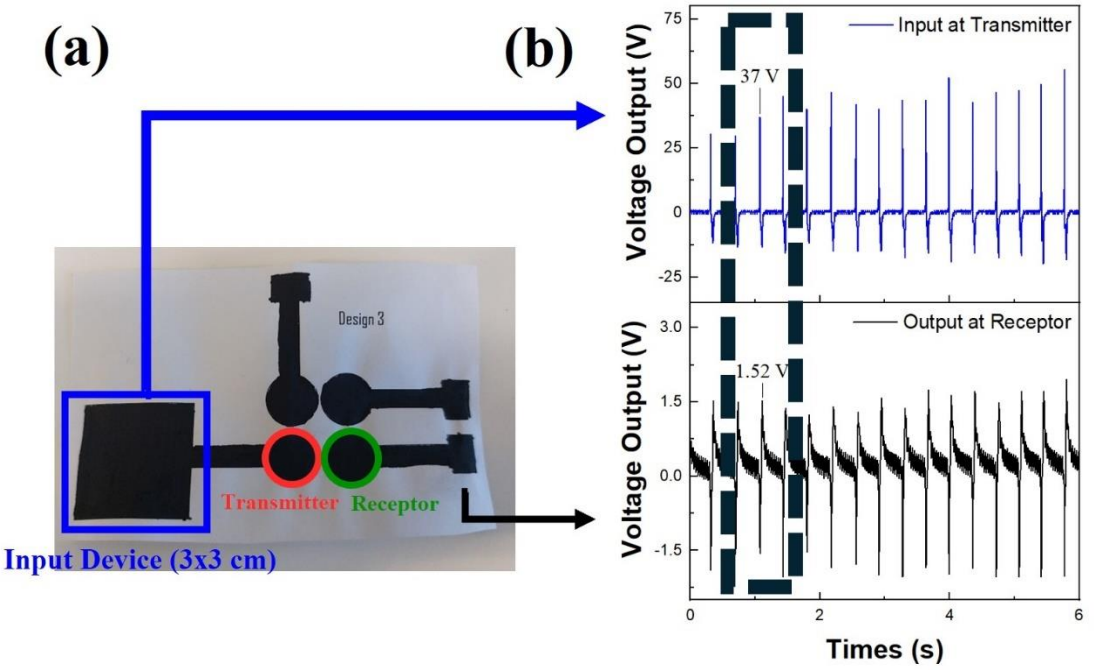

Figure 3.3.1.1 — Antenna Designs Efficiency Analysis: (a) Patterned Design 3, (b) Transmitter output and Receptor output associated with produced Design 3.

A summary of the results obtained for each design is presented in Figure 3.3.1.2. The analysis of these results revealed that the efficiencies, in ascending order, are as it follows Design 1 (1.11%), Design 4 (1.25%), Design 6 (1.33%), Design 5 (1.64%), Design 2 (2.44%), Design 7 (2.51%), Design 8 (2.83%), Design 9 (3.01%), and Design 3 (3.75%). In an initial analysis of the results, it becomes clear that as both the transmitter and/or receptor increase in size, so does the efficiency. Upon further analysis, it is possible to observe that changes in the transmitter size and the receptor have different impacts on the overall efficiency of the design.

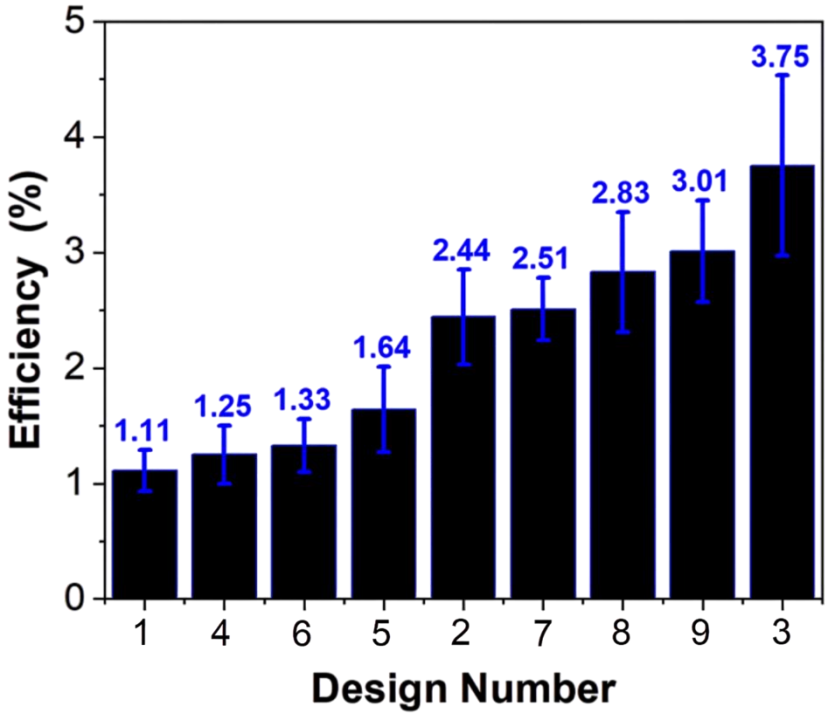

Figure 3.3.1.2 — Antenna Designs Efficiencies: Summary of the different efficiencies obtained through geometry changes between the different designs proposed.

In order to attest to this phenomenon, we can consider, for example, design number 4 and 5. Although in both cases one of the structures, either transmitter or receptor, measure 0.5 cm^2 and 1 cm^2, Design 4 presents an efficiency of 1.25%, while Design 5 presents an efficiency of 1.64%. The difference here is that in Design 5 the transmitter is the one measuring 1 cm^2, while in Design 4 it measures 0.5 cm^2. This correlation can be observed for any pair of structures with interchangeable transmitter and receptor sizes, indicating that increases in the transmitter structure is more prominent to increase efficiency than size increases in the receptor.

This statement can be further substantiated by analyzing the change in efficiency between Design 1 and Design 7, compared to the change in efficiency between Design 1 and Design 6. In the first case, for both the designs the receptor measures 0.5 cm^2, while the transmitter structure goes from 0.5 cm^2 in Design 1, to 1.5 cm^2 in Design 7, increasing the structure efficiency from 1.11% to 2.51% (a 126% increase). In the other hand, as the transmitter structure remains at 0.5 cm^2, while the receptor size goes from 0.5 cm^2 in Design 1, to 1.5 cm^2 in Design 6, the efficiency only increases from 1.11% to 1.33% (a 19% increase).

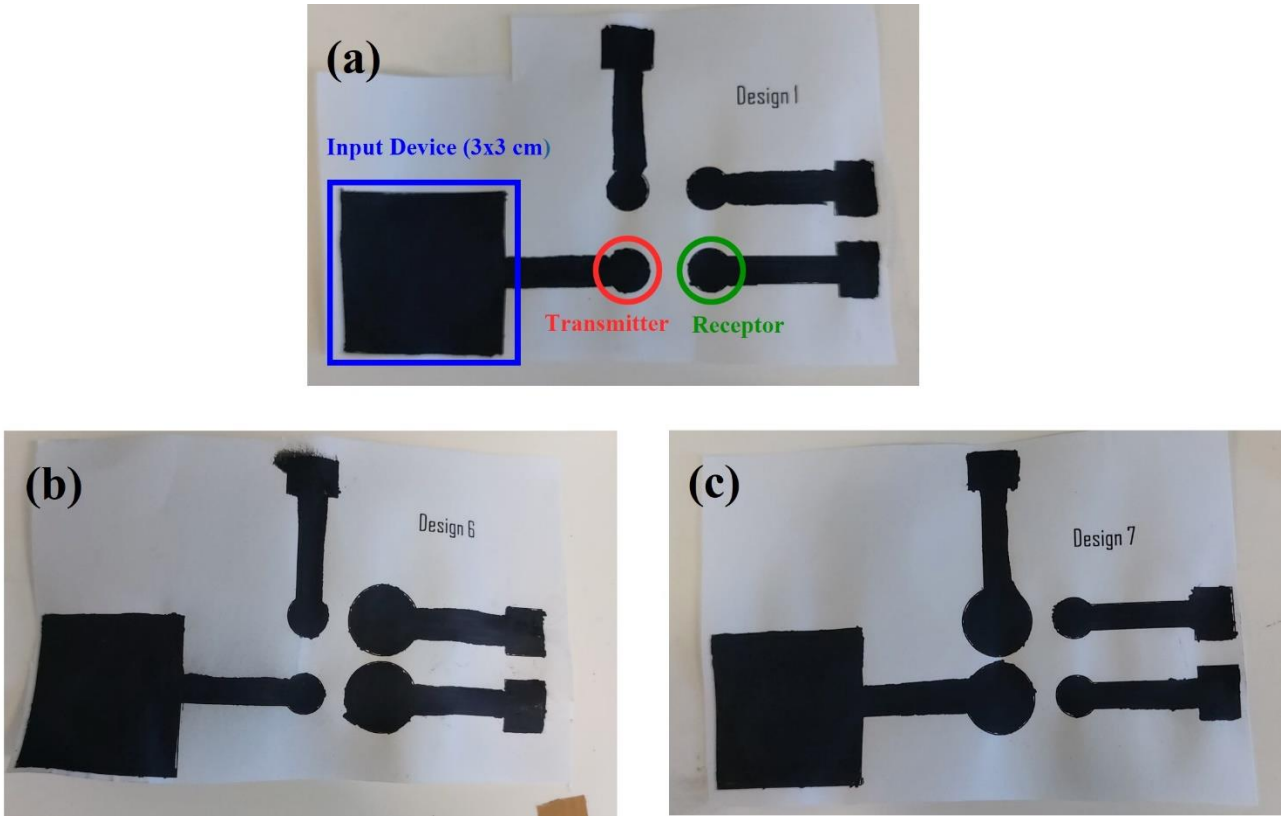

Figure 3.3.1.3 — Antenna Patterned Designs: (a) Design 1 with both transmitter and receptor circular structures measuring 0.5 cm^2; (b) Design 6 with transmitter measuring 0.5 cm^2 and receptor measuring 1.5 cm^2; (c) Design 7 with transmitter measuring 1.5 cm^2 and receptor measuring 0.5 cm^2.

3.4 MXene Paper-based Humidity Sensor

3.4.1 Silver Interdigitated Electrode Patterning

Considering that the proposed humidity sensing device consists of the deposition of MXene functional ink layers on top of a paper-electrode structure, the patterning of the silver electrodes corresponds to the first stage of the development in the device production. These interdigitated electrodes were patterned through screen-printing technique onto the four different paper substrates previously mentioned: the office paper, and the three different Navigator™ raw paper substrates (40 g/m^2, 80 g/m^2, 100 g/m^2).

For this process, three samples for each of the paper substrates were prepared. As presented in Figure 3.4.1.1 each of these paper substrate samples measured 5x7.5 cm, allowing for the simultaneous patterning of 6 interdigitated electrode structures in each pass. This way was possible to achieve multiple available silver electrode samples, within which the best ones for a given paper substrate, were selected to compose the device. As such, per paper substrate analyzed during the course of this research there were always multiple devices produced under the exact same conditions, in the attempt of reducing variability issues.

The main concerns during the deposition of electrodes were to ensure a homogeneous spread of the silver ink, a smooth surface, and well defined edges on the pattern, ensuring a highly conductive and robust electrode structure. Achieving these demanding requirements for the electrodes was essential, as these represented the only point of contact between the device enclosed in the humidity chamber and the exterior, where

the data related to the changes on the electrical impedance as a function RH was being collected and analyzed. The existence of discontinuities on the pattern, lack of adhesion to the substrate, bridging defects, or any other defect, could compromise performance results obtained, by promoting inconsistent sensing performance, degraded signal quality and overall device durability.

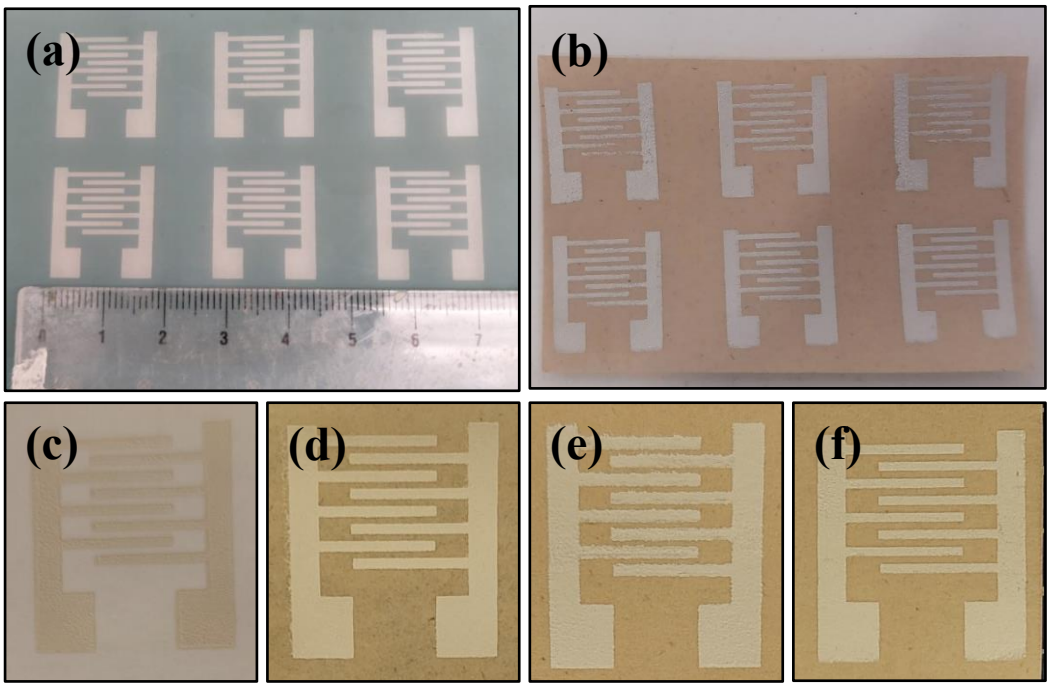

Figure 3.4.2.1 — Silver Ink Electrodes Patterning Results: (a) Screen-printing mesh employed in electrodes patterning; (b) Office paper substrate sample with 6 electrode structure printed; (c) Silver ink interdigital electrode patterned on office paper substrate; (d)) Silver ink interdigital electrode patterned on Navigator™ 40 g/m^2 substrate; (e) Silver ink interdigital electrode patterned on Navigator™ 80 g/m^2 substrate; (f) Silver ink interdigital electrode patterned on Navigator™ 100 g/m^2 substrate.

3.4.2 MXene Functional Ink Deposition

Following the paper-electrode structure preparation, it was required to incorporate the layers of MXene functional ink, providing increased humidity sensing capabilities to the device. Bearing performance in mind, it was attempted to achieve a homogeneous, compact, sufficiently thick layer of functional ink, allowing for optimized surface area, uniform/accurate response, and mechanical stability which can be associated with reliability and durability of the device.

The main concern in this stage of development was to cover the superior part of the silver electrodes in its entirety, providing maximum contact area between the chamber environment, the functional ink, and silver electrodes. This way was possible to maintain the final device size small, while allowing for its effective operation. The lower part of the electrode structure was left uncovered, allowing to connect the device to the measuring equipment's, and retrieve the electrical impedance data during testing phase. Due to the unavailability of a screen-printing mesh with a squared pattern correctly sized for the MXene top layer, the incorporation of the layer was done through the use of a painting brush. This way was possible to administrate a controlled amount of ink in each passage, while also allowing for a relatively homogenous layer to be put in place and preserving the integrity of the contacts in a simple, fast, and cheap way.

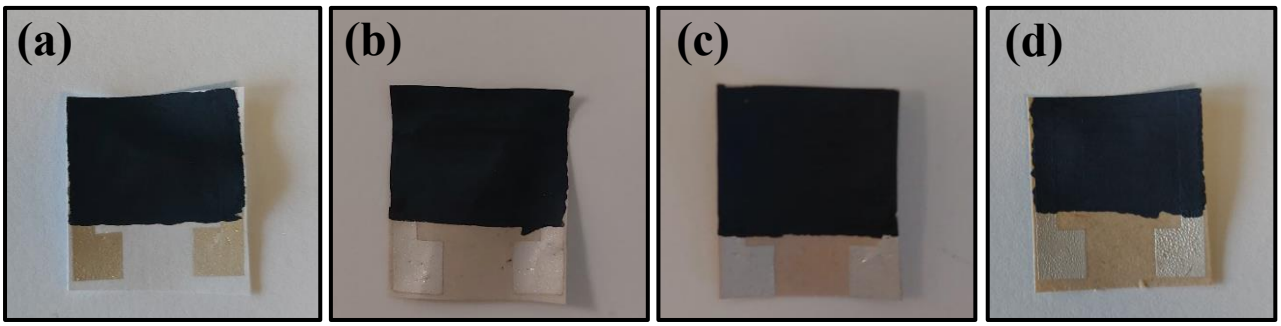

Figure 3.4.2.1 — Produced Humidity Sensing Devices: (a) MXene sensing layer on office paper based device; (b) MXene sensing layer on Navigator™ 40g/m^2 paper based device; (c) MXene sensing layer on Navigator™ 80g/m^2 paper based device (d) MXene sensing layer on Navigator™ 100g/m^2 paper based device.

Considering the resistive principle in which this device is based on, but also concerns related to sensitivity, accuracy and durability, certain characteristics in the final devices were mandatory. Among those, a high conductivity MXene layer and thick uniform coverage of the paper-electrode structure were prioritized. This way was possible to ensure the highest degree of performance and durability given the materials and design of the device. From Figure 3.4.2.2, it is possible to analyze the impact of the increasing number of layers did on the coverage density of the substrate for the office paper based device.

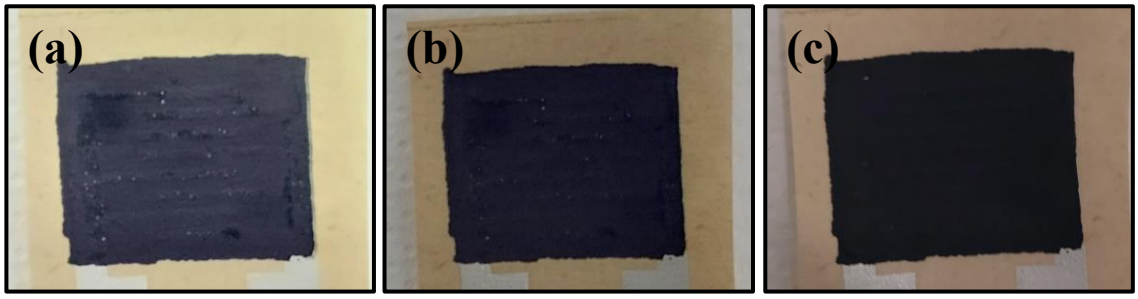

Figure 3.4.2.2 — **MXene Layer Deposition Results:** (a) MXene sensing layer on office paper based device; (b) MXene sensing layer on Navigator™ 40g/m^2 paper based device; (c) MXene sensing layer on Navigator™ 80g/m^2 paper based device; (d)) MXene sensing layer on Navigator™ 100g/m^2 paper based device.

There is a noticeable and progressive decrease of exposed areas, which would have led to sensitivity, accuracy and overall signal quality and fidelity issues. This way a minimum of three layers was employed in the development of each of the sensors. After all the conductive layers were place and dried, the total thickness and resistance of the device was determined.

Table 3 - Antenna Design Thickness and Resistance

Paper Substrate Utilized	Thickness (μm)*	Resistance (Ω)**
Navigator™ 40g/m^2	91 ±0.5	5.7±1.2
Navigator™ 80g/m^2	104 ±0.5	9.4 ± 2.1
Navigator™ 100g/m^2	115 ±0.5	5.2±1.7
Office Paper 80g/m^2	116 ±0.5	8.6 ±0.6

***Note:** The thickness was measured through the use of a digital micrometer. ** The resistance was measured utilizing a multimeter, placing the testing probes on the center of the exposed end of the silver ink contacts.

3.4.3 Humidity Sensing Performance

In order to attest to the humidity sensing capabilities of the produced devices, these were inserted one at a time inside a humidity chamber, and the resistance values were registered as the RH levels varied. The proposed cycle comprehended an increase in RH levels from 10% up to 60%, and then a decrease, back to 10%, once the 60% peak was reached. This way was possible to determine the variation in resistance of the device with increasing RH, and its recovery ability through the second part of the cycle when the RH levels diminished from 60% to 10%. Due to technical limitations of the equipment, the minimum and maximum attained RH levels slightly differed from measure to measure.

For these measurements the devices were inserted in a voltage divider circuit, where an input voltage of 5 V was forced, and a fixed resistance of 100 KΩ added. Given this set up, by measuring the voltage between the device ends, was possible to determine the resistance of the device at any given moment. The purpose of the voltage divider circuit was to adjust the sensibility of the device. In other words, by adjusting the fixed resistance value, it would be possible to have more pronounced variations in the device resistance value with the same changes in RH. For this research the 100 kΩ was deemed adequate, given the results obtained. Due to the use of different paper substrates for each device, different behaviors were observed. The results obtained for each of the devices are presented in Figure 3.4.3.1, where the black lines indicate the resistance variation in the device and the blue lines correspond to the RH variation in the environmental chamber.

For the humidity sensor based on the 80 g/m^2 office paper, the resistance decreases from 45.36 Ω at a RH level of 20.4% to 42.85 Ω when the RH reaches the 60% mark. Although the RH level starts to decrease after reaching the 60% peak, as it can be observed, for this device the resistance continues to decrease until the end of the measurement, presenting at a resistance value of 40.85 Ω, by the end of the measurement, at which point the RH is approximately 20%. A similar behavior is observed when analyzing the data related with the Navigator™ 100 g/m^2 based device. The resistance value decreases from approximately 43.00 Ω at a RH level of 19.35%, down to 40.90 Ω when the RH level reaches 60%, and keeps decreasing until the end of the measurement, reaching a value of 38.65 Ω when the RH is reduced to 19.92%.

As we move towards the samples based of the more porous paper substrates, in particular the Navigator™ 80 g/m^2 and Navigator™ 40 g/m^2, a change in behavior is observed. Starting with the Navigator™ 80 g/m^2 based device, as the RH levels go from 15.09 % up to 64% the device resistance decreases from 47.02 Ω to 43.90 Ω, respectively. Similar to the previous cases the resistance still decreases after the 60% peak is reached, although this decrease does not continue until the end of the measurement, as the resistance value starts to stabilize 2 hours after peak RH conditions are reached. From said point forward the resistance of the device remains close to 43.75 Ω. Finally, for the Navigator™ 40 g/m^2 based device, initially the resistance value decreases from 47.02 Ω to 43.90 Ω as the RH levels increase from 15.09% up to 64%. As the 60% RH peak is reached, the resistance of the device starts increasing, as the RH levels decrease in the second stage of the cycle, indicating recovery capabilities. For this device, the resistance increases from 42.97 Ω to 49.14 Ω as the RH levels return from 64.14% to 21.86%.

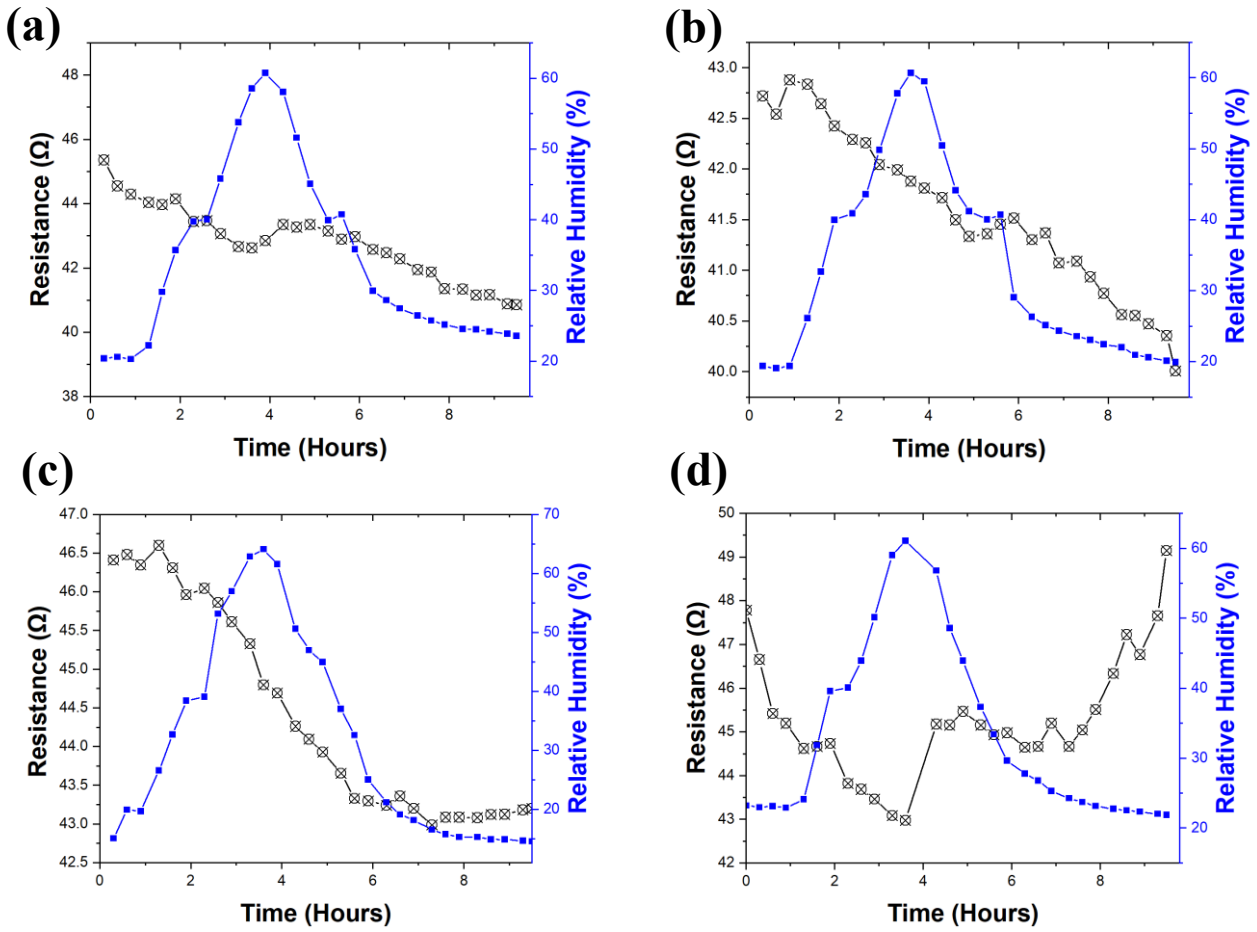

Figure 3.4.3.1 — Humidity Sensing Results: (a) MXene sensing layer on office paper-based device; (b) MXene sensing layer on Navigator™ 100 g/m^2 paper-based device. (c) MXene sensing layer on Navigator™ 80 g/m^2 paper-based device; (d) MXene sensing layer on Navigator™ 40 g/m^2 paper-based device.

The change in behavior resulting from the use of different paper-based substrates is most likely due to distinct water adsorption, absorption and retention tendencies. Changes in the chemical treatments, surface morphology, and porosity between the various paper-based substrates employed, cause changes in terms of the required time for adsorption, absorption, and desorption of water molecules from the cellulose structure, leading to different moisture retention behaviors [50]. As a result, for the office paper and Navigator™ 100 g/m^2, the device resistance keeps decreasing even after the RH levels reach a maximum and start to decrease. Due to the smaller porous sizes of these substates the period of time required to promote a complete adsorption, absorption and desorption of moisture is higher. As RH levels increase during the first half of the cycle water molecules accumulate at the paper surface (adsorption), taking time to be drawn to the bulk of the substrate (absorption), as well as to leave the surface and internal cellulose structure (desorption). Consequently, as the RH levels start to decrease in the second stage of the cycle, there is still moisture accumulated form the first half of the cycle, retained inside the substrate, and resistance remains low as the moisture continues to facilitate the conduction withing the device. This phenomenon is partially mitigated as the substrate porous sizes increase, promoting a more effective and immediate interchange of water moisture with the environment. Once again, this supposition is supported by resistance stabilization for the Navigator™ 80 g/m^2, and reversible behavior of the Navigator™ 40 g/m^2 based sample, which corresponds to the substrate with the biggest porous size.

4

CONCLUSION AND FUTURE PERSPECTIVES

The aim of this research was to optimize the composition, production, and patterning of Ti_3C_2-based functional ink on paper substrates, attempting for the production of sensitive, nontoxic, eco-friendly, low-cost, flexible paper-based antennas, and humidity sensors, for possible future applications in intelligent packaging.

With this goal in mind, MXene stock solution was produced, and the success of this process was assessed through a set of chemicals, physical, and optical analysis, including FITR, XRD, Raman, and UV-VIS-NIR Spectroscopy. The presence of -OH, -F, and -O functional groups, as well as, typical MXene related bonds was confirmed, indicating correct production of the MXene base solution. From said solution different functional inks were prepared and based on the rheological properties associated with each of the samples, the denominated MXene Ink 2, was determined to be the most adequate for both screen-printing and other patterning techniques considered, such as hand pattering through ink pen.

As for the production of the proposed devices, the first stage was related with the development of a self-powered circuit, namely a low-cost, simple, and efficient TENG structure. In order to accomplish this, a paper sample, measuring 3x3 cm, coated with multiple layers of MXene functional ink, was combined with a PDMS sheet of the same size. This combination provided a flexible and stable substrate through the use of paper, a highly conductive electrode layer, form the MXene layers, and an effective triboelectric layer due to the use of PDMS. The output dependency on force and frequency of impact was studied and was possible to conclude that with both an increase of impact force and frequency of impact the voltage output increases. Given the conditions employed, a maximum average output of 52.02 ± 0.49 V, for an impact force of 80N at 2 Hz. As for the power and current density, the results revealed that the peak power density and current density, for an applied force of 20 N at 2 Hz, were approximately 17 mA/m^2 and 0.26 W/m^2, respectively. This triboelectric behavior was employed as input for the analysis of the antenna's performance.

The performance associated with different antenna designs, comprehending changes in terms of the circular transmitter and receptor areas, was verified. The results allowed to corroborate that altering the geometry of patch antennas influences their performance and indicated a distinct impact of changes in the transmitter or receptor. According to the results, increases in the transmitter area have greater impact in the increase of the antenna efficiency, when compared to similar size increases on the receptor. The best performing antenna presented an efficiency of approximately 3.75%.

As for the humidity sensing capabilities of the paper-based humidity sensors produced, not only the use of MXene was considered, but also the impact of different paper substrates would have in the sensing capabilities. In total, five different devices, with five distinct cellulose substrates, were analyzed. Different device

resistance behaviors were observed for the samples based on office paper weighing 80 g/m^2, and Navigator™ raw paper substrates weighing 40 g/m^2, 80 g/m^2, 100 g/m2. In the bases of the distinct results, were, most likely, different water adsorption, absorption and retention tendencies, due to changes in the porous structures form substrate to substrate.

Taking into consideration the results obtained throughout this research, in subsequent stages of development, the different produced devices could be further analyzed and adapted towards specific uses. In terms of the TENG structure it would be important to attest the dependency on a wider range of impact forces and impact frequencies, in order to access the limits of operation of the device. Additionally, the potential usage of this triboelectric structure for powering small electronics, such as LEDs, could be of interest. As for the antenna designs, in order to fully implement them in intelligent packaging solutions, the designs would have to be adapted to RFID specific layouts, or similar, and the structure functionality proven. Given the principle of operation of passive RFID tags, based on current induction through an electromagnetic field generated by the reader's antenna, the high conductivity of MXene seems, theoretically, capable of capturing the electromagnetic energy, but it also has to be able to reflect the signal back to the reader. Both capabilities require further analysis. If functional, these structures could be utilized as part of intelligent packaging solutions for tracking, authentication, and monitoring purposes. For the humidity sensors, the results demonstrated that the only device capable of recovering throughout the RH variations, was the one associated with the lightest of all the substrates tested, the Navigator™ 40 g/m^2. This may be problematic considering the durability of the device, as such, adaptations on the functional ink, for example the inclusion of salt solutions, should be addressed in the attempt to produce sensitive and precise devices based on more durable paper substrates. Additionally, the range of operation of these devices should be further tested, analyzing the response throughout wider RH ranges, such as 10% to 85%. It is important to notice that the set-up utilized, makes the humidity results obtained dependent on the fixed resistance utilized, and consequently, further studies of the humidity sensor response without recourse to a voltage divider circuit, is yet to be determined. Furthermore, research towards the development of combined antenna and sensor devices would provide a more ideal solution for intelligent packaging.

BIBLIOGRAPHY

[1] H. M. C. Azeredo and D. S. Correa, "Smart choices: Mechanisms of intelligent food packaging," *Curr Res Food Sci*, vol. 4, pp. 932–936, Jan. 2021, doi: 10.1016/J.CRFS.2021.11.016.

[2] "How Iot and Sensors Are Revolutionizing Industrial Packaging." Accessed: Sep. 22, 2024. [Online]. Available: https://www.greenlivingblog.org.uk/future-of-smart-packaging-with-iot-and-sensors/

[3] L. Wang, Z. Wu, and C. Cao, "Technologies and Fabrication of Intelligent Packaging for Perishable Products," *Applied Sciences 2019, Vol. 9, Page 4858*, vol. 9, no. 22, p. 4858, Nov. 2019, doi: 10.3390/APP9224858.

[4] A. Petrillo, F. De Felice, R. Cioffi, and F. Zomparelli, "Fourth Industrial Revolution: Current Practices, Challenges, and Opportunities," *Digital Transformation in Smart Manufacturing*, Feb. 2018, doi: 10.5772/INTECHOPEN.72304.

[5] "Advanced Technologies for Industry-Product Watch Flexible and printed electronics," 2021, doi: 10.2826/295137.

[6] M. Li and Q. Wang, "Will technology advances alleviate climate change? Dual effects of technology change on aggregate carbon dioxide emissions," *Energy for Sustainable Development*, vol. 41, pp. 61–68, Dec. 2017, doi: 10.1016/J.ESD.2017.08.004.

[7] A. A. Fawole, O. Felix Orikpete, N. N. Ehiobu, D. Raphael, and E. Ewim, "Climate change implications of electronic waste: strategies for sustainable management," *Bulletin of the National Research Centre 2023 47:1*, vol. 47, no. 1, pp. 1–10, Oct. 2023, doi: 10.1186/S42269-023-01124-8.

[8] X. Guan *et al.*, "Flexible humidity sensor based on modified cellulose paper," *Sens Actuators B Chem*, vol. 339, p. 129879, Jul. 2021, doi: 10.1016/J.SNB.2021.129879.

[9] Y. U. Haq *et al.*, "Synthesis and characterization of 2D MXene: Device fabrication for humidity sensing," *Journal of Science: Advanced Materials and Devices*, vol. 7, no. 1, p. 100390, Mar. 2022, doi: 10.1016/J.JSAMD.2021.08.003.

[10] "THE 17 GOALS | Sustainable Development." Accessed: Aug. 09, 2024. [Online]. Available: https://sdgs.un.org/goals

[11] E. Fortunato, N. Correia, P. Barquinha, L. Pereira, G. Goncalves, and R. Martins, "High-performance flexible hybrid field-effect transistors based on cellulose fiber paper," *IEEE Electron Device Letters*, vol. 29, no. 9, pp. 988–990, 2008, doi: 10.1109/LED.2008.2001549.

[12] C. Lin *et al.*, "Development progress, performance enhancement routes, and applications of paper-based triboelectric nanogenerators," *Chemical Engineering Journal*, vol. 430, p. 132559, Feb. 2022, doi: 10.1016/J.CEJ.2021.132559.

[13] C. Xiong, T. Wang, J. Han, Z. Zhang, and Y. Ni, "Recent Research Progress of Paper-Based Supercapacitors Based on Cellulose," *Energy & Environmental Materials*, p. e12651, 2023, doi: 10.1002/EEM2.12651.

[14] Y. Zhang *et al.*, "Flexible paper-based ZnO nanorod light-emitting diodes induced multiplexed photoelectrochemical immunoassay," *Chemical Communications*, vol. 50, no. 12, pp. 1417–1419, Jan. 2014, doi: 10.1039/C3CC48421A.

[15] P. B. Deroco, D. Wachholz Junior, and L. T. Kubota, "Paper-based Wearable Electrochemical Sensors: A New Generation of Analytical Devices," *Electroanalysis*, vol. 35, no. 1, p. e202200177, Jan. 2023, doi: 10.1002/ELAN.202200177.

[16] Y. Zhang *et al.*, "Flexible Electronics Based on Micro/Nanostructured Paper," *Advanced Materials*, vol. 30, no. 51, p. 1801588, Dec. 2018, doi: 10.1002/ADMA.201801588.

[17] "Printed Electronics Market Size to Hit USD 83.77 Bn by 2034." Accessed: Oct. 07, 2024. [Online]. Available: https://www.precedenceresearch.com/printed-electronics-market

[18] Y. Pei *et al.*, "Ti3C2TXMXene for Sensing Applications: Recent Progress, Design Principles, and Future Perspectives," *ACS Nano*, vol. 15, no. 3, pp. 3996–4017, Mar. 2021, doi: 10.1021/ACSNANO.1C00248/ASSET/IMAGES/LARGE/NN1C00248_0016.JPEG.

[19] A. Bolotsky *et al.*, "Two-Dimensional Materials in Biosensing and Healthcare: From in Vitro Diagnostics to Optogenetics and beyond," *ACS Nano*, vol. 13, no. 9, pp. 9781–9810, May 2019, doi: 10.1021/ACSNANO.9B03632/ASSET/IMAGES/LARGE/NN9B03632_0009.JPEG.

[20] M. Naguib *et al.*, "Two-Dimensional Nanocrystals Produced by Exfoliation of Ti3AlC2," *Advanced Materials*, vol. 23, no. 37, pp. 4248–4253, Oct. 2011, doi: 10.1002/ADMA.201102306.

[21] Z. Yang *et al.*, "Improvement of gas and humidity sensing properties of organ-like mxene by alkaline treatment," *ACS Sens*, vol. 4, no. 5, pp. 1261–1269, May 2019, doi: 10.1021/ACSSENSORS.9B00127/ASSET/IMAGES/LARGE/SE-2019-00127Z_0008.JPEG.

[22] F. R. Fan, Z. Q. Tian, and Z. Lin Wang, "Flexible triboelectric generator," *Nano Energy*, vol. 1, no. 2, pp. 328–334, Mar. 2012, doi: 10.1016/J.NANOEN.2012.01.004.

[23] Y. Wang, Y. Yang, and Z. L. Wang, "Triboelectric nanogenerators as flexible power sources," *npj Flexible Electronics 2017 1:1*, vol. 1, no. 1, pp. 1–10, Nov. 2017, doi: 10.1038/s41528-017-0007-8.

[24] Y. Zhang *et al.*, "Flexible Electronics Based on Micro/Nanostructured Paper," *Advanced Materials*, vol. 30, no. 51, p. 1801588, Dec. 2018, doi: 10.1002/ADMA.201801588.

[25] R. Carvalho *et al.*, "Improving the Performance of Paper-Based Dipole Antennas by Electromagnetic Flux Concentration," *ACS Appl Mater Interfaces*, vol. 15, no. 8, pp. 11234–11243, Mar. 2023, doi: 10.1021/ACSAMI.2C19889/SUPPL_FILE/AM2C19889_SI_001.MP4.

[26] M. M. Tentzeris, "Novel paper-based inkjet-printed antennas and wireless sensor modules," *2008 IEEE International Conference on Microwaves, Communications, Antennas and Electronic Systems, COMCAS 2008*, 2008, doi: 10.1109/COMCAS.2008.4562792.

[27] M. Ahmad *et al.*, "Paper-Based Printed Antenna: Investigation of Process-Induced and Climatic-Induced Performance Variability," *Adv Eng Mater*, vol. 25, no. 16, p. 2201703, Aug. 2023, doi: 10.1002/ADEM.202201703.

[28] B. Sindhu, V. Adepu, P. Sahatiya, and S. Nandi, "An MXene based flexible patch antenna for pressure and level sensing applications," *FlatChem*, vol. 33, p. 100367, May 2022, doi: 10.1016/J.FLATC.2022.100367.

[29] Y. sheng Wang *et al.*, "Carrageenan-modified MXene nanocomposite-based all-printed flexible humidity sensor for healthcare application," *Sens Actuators B Chem*, vol. 418, p. 136316, Nov. 2024, doi: 10.1016/J.SNB.2024.136316.

[30] X. Guan *et al.*, "Flexible humidity sensor based on modified cellulose paper," *Sens Actuators B Chem*, vol. 339, p. 129879, Jul. 2021, doi: 10.1016/J.SNB.2021.129879.

[31] T. Delipinar, A. Shafique, M. S. Gohar, and M. K. Yapici, "Fabrication and Materials Integration of Flexible Humidity Sensors for Emerging Applications," *ACS Omega*, vol. 6, no. 13, pp. 8744–8753, Apr. 2021, doi: 10.1021/ACSOMEGA.0C06106.

[32] H. wen Zhang *et al.*, "Interlayer cross-linked MXene enables ultra-stable printed paper-based flexible sensor for real-time humidity monitoring," *Chemical Engineering Journal*, vol. 495, p. 153343, Sep. 2024, doi: 10.1016/J.CEJ.2024.153343.

[33] M. Alhabeb *et al.*, "Guidelines for Synthesis and Processing of Two-Dimensional Titanium Carbide (Ti3C2Tx MXene)," *Chemistry of Materials*, vol. 29, no. 18, pp. 7633–7644, Sep. 2017, doi: 10.1021/ACS.CHEMMATER.7B02847/ASSET/IMAGES/LARGE/CM-2017-02847C_0005.JPEG.

[34] T. Zhang *et al.*, "Synthesis of two-dimensional Ti3C2Tx MXene using HCl+LiF etchant: Enhanced exfoliation and delamination," *J Alloys Compd*, vol. 695, pp. 818–826, Feb. 2017, doi: 10.1016/J.JALLCOM.2016.10.127.

[35] S. Abdolhosseinzadeh, X. Jiang, H. Zhang, J. Qiu, and C. (John) Zhang, "Perspectives on solution processing of two-dimensional MXenes," *Materials Today*, vol. 48, pp. 214–240, Sep. 2021, doi: 10.1016/J.MATTOD.2021.02.010.

[36] W. He, M. Sohn, R. Ma, and D. J. Kang, "Flexible single-electrode triboelectric nanogenerators with MXene/PDMS composite film for biomechanical motion sensors," *Nano Energy*, vol. 78, Dec. 2020, doi: 10.1016/J.NANOEN.2020.105383.

[37] G. Liu *et al.*, "Polyelectrolyte functionalized ti2ct x mxene membranes for pervaporation dehydration of isopropanol/water mixtures," *Ind Eng Chem Res*, vol. 59, no. 10, pp. 4732–4741, Mar. 2020, doi: 10.1021/ACS.IECR.9B06881.

[38] A. Rozmysłowska-Wojciechowska *et al.*, "Engineering of 2D Ti3C2 MXene Surface Charge and its Influence on Biological Properties," *Materials 2020, Vol. 13, Page 2347*, vol. 13, no. 10, p. 2347, May 2020, doi: 10.3390/MA13102347.

[39] S. Kumar, H. M. Park, T. Singh, M. Kumar, and Y. Seo, "Long-Term Stability Studies and Applications of Ti3C2Tx MXene," *Int J Energy Res*, vol. 2023, no. 1, p. 5275439, Jan. 2023, doi: 10.1155/2023/5275439.

[40] A. Rawat *et al.*, "Investigation of charge carrier dynamics in a Ti 3 C 2 T x MXene for ultrafast photonics applications," *Mater Adv*, vol. 4, no. 23, pp. 6427–6438, Nov. 2023, doi: 10.1039/D3MA00429E.

[41] S. A. Melchior *et al.*, " High-Voltage Symmetric Supercapacitor Based on 2D Titanium Carbide (MXene, Ti 2 CT x)/Carbon Nanosphere Composites in a Neutral Aqueous Electrolyte ," *J Electrochem Soc*, vol. 165, no. 3, pp. A501–A511, 2018, doi: 10.1149/2.0401803JES.

[42] E. Satheeshkumar, T. Makaryan, A. Melikyan, H. Minassian, Y. Gogotsi, and M. Yoshimura, "One-step Solution Processing of Ag, Au and Pd@MXene Hybrids for SERS," *Sci Rep*, vol. 6, Aug. 2016, doi: 10.1038/SREP32049.

[43] T. Malina *et al.*, "Tuning the transformation and cellular signaling of 2D titanium carbide MXenes using a natural antioxidant," *Matter*, vol. 7, no. 1, pp. 191–215, Jan. 2024, doi: 10.1016/J.MATT.2023.10.026.

[44] H. W. Lin, C. P. Chang, W. H. Hwu, and M. Der Ger, "The rheological behaviors of screen-printing pastes," *J Mater Process Technol*, vol. 197, no. 1–3, pp. 284–291, Feb. 2008, doi: 10.1016/J.JMATPROTEC.2007.06.067.

[45] C. Xu and N. Willenbacher, "How rheological properties affect fine-line screen printing of pastes: a combined rheological and high-speed video imaging study," *J Coat Technol Res*, vol. 15, no. 6, pp. 1401–1412, Nov. 2018, doi: 10.1007/S11998-018-0091-2.

[46] K. Možina and V. Rutar, "Comparison Of Conventional And Recycled 'Green' Office Paper," *Journal of Graphic Engineering and Design*, vol. 2, no. 1, pp. 38–45, Jun. 2011, doi: 10.24867/JGED-2011-1-038.

[47] E. Jansson *et al.*, "Suitability of Paper-Based Substrates for Printed Electronics," *Materials 2022, Vol. 15, Page 957*, vol. 15, no. 3, p. 957, Jan. 2022, doi: 10.3390/MA15030957.

[48] M. S. Rasel, H. O. Cho, J. W. Kim, and J. Y. Park, "A self-powered triboelectric sensor for wide-range pressure detection in wearable application," *J Phys Conf Ser*, vol. 1052, no. 1, Jul. 2018, doi: 10.1088/1742-6596/1052/1/012029.

[49] K. Paramayudha, A. B. Santiko, Y. Wahyu, F. Oktafiani, A. Fitriadi, and H. Wijanto, "Design and realization of circular patch antenna for S-Band Coastal Radar," *Proceeding - 2016 International Conference on Radar, Antenna, Microwave, Electronics, and Telecommunications, ICRAMET 2016*, pp. 115–118, Feb. 2017, doi: 10.1109/ICRAMET.2016.7849595.

[50] A. Etale, A. J. Onyianta, S. R. Turner, and S. J. Eichhorn, "Cellulose: A Review of Water Interactions, Applications in Composites, and Water Treatment," *Chem Rev*, vol. 123, no. 5, p. 2016, Mar. 2023, doi: 10.1021/ACS.CHEMREV.2C00477.

[51] G. Ferreira, S. Goswami, S. Nandy, L. Pereira, R. Martins, and E. Fortunato, "Touch-Interactive Flexible Sustainable Energy Harvester and Self-Powered Smart Card," *Adv Funct Mater*, vol. 30, no. 5, Jan. 2020, doi: 10.1002/ADFM.201908994.

A

APPENDIX 1: TENG STRUCTURE AND ANTENNA DESIGN

In this project, for the production of a functional TENG structure, a paper substrate sample was coated with layers of MXene functional ink and paired with a PDMS sheet, placed on top of the structure. In this case, the paper substrate provided support and structure to the device, the MXene ink layer worked as a conductive electrode layer, while the PDMS acted as a charge generating layer.

For this structure the open-circuit voltage (V_{OC}) output variation based on applied force and frequency of impact was determined. Maintaining the impact frequency at 2 Hz, the output obtained through the use of an impact force of 20 N, was on average 21.2 ± 0.5 V. As the impact force increased to 40 N the average output voltage also increased to 34.0 ± 0.5 V. As we moved up towards 60 N, the output voltage value increased once again, to an average value of 44.0 ± 0.4 V. Finally, for the last force value tested, 80 N, the average output voltage value was determined to be 52.0 ± 0.5 V. As for the output dependency on impact frequency, maintaining the impact force at 40 N, while using a 1 Hz impact frequency, the average output voltage obtained was 32.6 ± 0.4 V. As the impact frequency changes to 2 Hz the average output voltage was, as presented before, 34.0 ± 0.5 V. As for the last case, utilizing an impact frequency of 3 Hz, the average output voltage value increased to 38.3 ± 0.5 V.

These results can be compared to different TENG structures previously analyzed. We can consider a 2 x 3 cm TENG structure based on a PANi/cellulose composite, tapped together to a metallic electrode (paper-based). In this structure a charge generating layer and conductive electrode layer are represented by the two different structures, respectively [51]. In terms of V_{OC} output variation based on applied force and frequency of impact, the results are within the same order of magnitude, but present considerable differences. Maintaining the impact frequency at 5 Hz, for an applied impact force of 8N, the obtained output was, on average, close to 25 V. As the impact force increased to 12 N the average output voltage also increased to around 64.0 V. With an impact force of 16 N, the output voltage value increased once again, attaining an average value of around 76 V. If we analyze the results obtained for the different impact frequencies, considering a fixed impact force of 16 N, while using a 1 Hz impact frequency, the average output voltage obtained was close to 52 V. As the impact frequency changes to 2 Hz the average output voltage was around 61 V. As for an impact frequency of 3 Hz, the average output voltage value increased around 70 V [51].

This shows the potential of the produced MXene/PDMS TENG structure explored in this project, and the existence of possible improvements through changes in the layers, in particular the charge generating layer, and the resulting synergy, leading to possible output values improvements.

As for the antenna designs, in order to better understand the performance of the device, the morphological properties of the deposited MXene ink layer were also attested through scanning electron microscopy (SEM). As it can be observed from Figure A1 (a), (b), the top view images indicate the presence of delaminated nanosheets, along with the presence of layered particles, distributed relatively evenly across the paper substrate, resulting in a dense and complete coverage. As for the cross section results, presented in Figure A1 (c), well defined and individualized layers can be observed, corresponding with the paper substrate and the MXene ink layer deposited on top. By analyzing this image through ImageJ free software, was possible to determine an average thickness for the paper substrate and MXene ink layer of and 83.83 ± 1.54 µm, respectively, leading to a total thickness of approximately 16 µm. These measurements support the device thickness values presented before in Table 2.

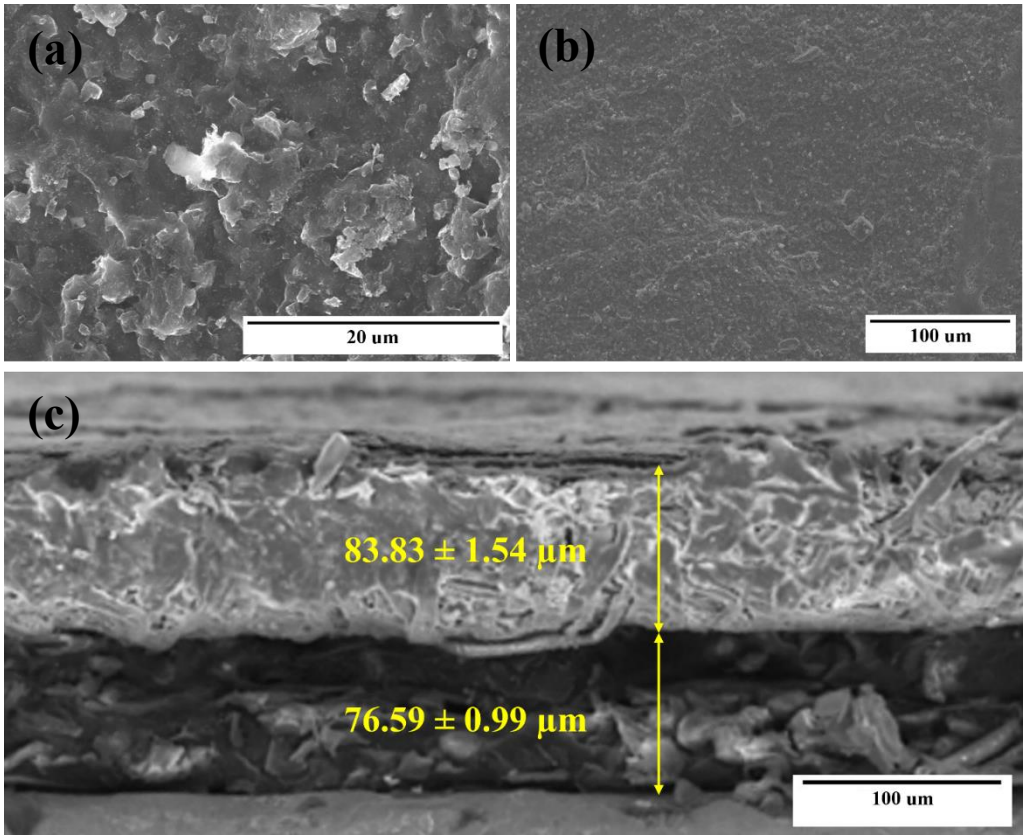

Figure A1 — **Scanning Electron Microscopy (SEM) images of the fabricated antennas:** (a) Top-view of the antenna sample at 2000x magnification, (b) Top-view of the antenna sample at 200x magnification, (c) Cross-section view of the antenna sample at 200x magnification.

An adaptation was also produced, and briefly analyzed. This new design corresponded to an attempt to integrate the produced MXene layer in a functional paper-based tag, developed in an independent project.

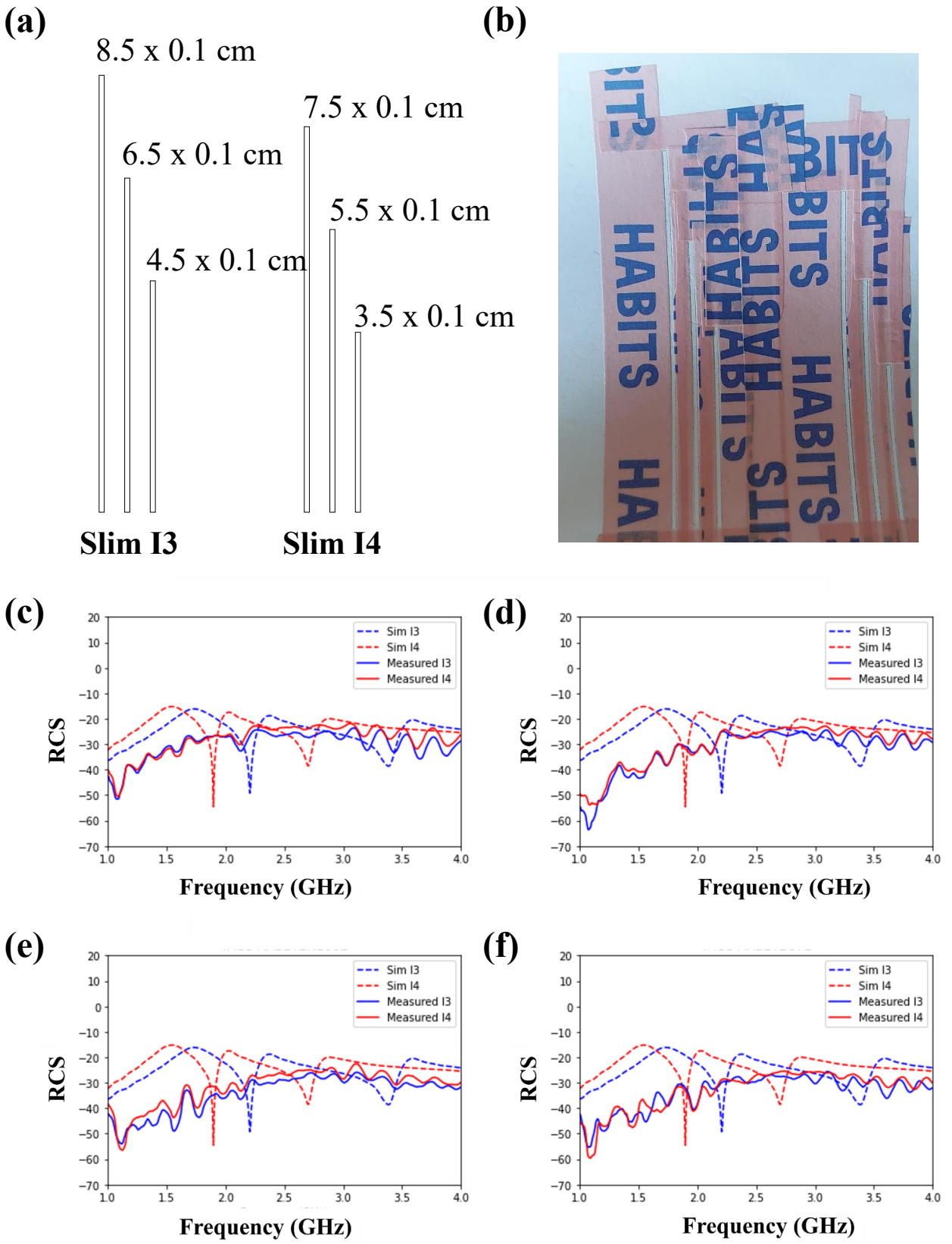

Figure A2 — Alternative Tag Design Production and Performance Analysis: (a) Denominated Slim I3 and Slim I4 tag designs and respective measurements, (b) Production of the device through paper tape patterning technique, (c) RCS versus Frequency analysis for Navigator™ 40 g/m^2 based device; (d)) RCS versus Frequency analysis for Navigator™ 80 g/m^2 based device, (e) RCS versus Frequency analysis for Navigator™ 100 g/m^2 based device, (f) RCS versus Frequency analysis for Office paper 80 g/m^2 based device.

The Radar Cross Section (RCS) response in function of the source frequency was evaluated and compared to the desired response, within the 1-5 GHz range, considering the proposed design and dimensions of the tag pattern. The RCS response allowed to determine what fraction of the electromagnetic energy the structure reflected back toward a radar source, accessing the scattering behavior of radiation associated with the produced design, a crucial parameter for the production of passive tags. For any of the produced antennas, all based on the same MXene ink but composed of different paper substrates, was there an indication of a response for the frequency values intended. The discussed reason behind the results obtained was related with insufficient conductivity of the ink, paired with the mate finish of the ink surface, which made it hard to promote efficient reflection of incident radiation. During the production of this tag design, the tape method was employed, due to the reduce dimensions of the structure, allowing to obtain straight, well defined, and very thin lines.

B

APPENDIX 2: HUMIDITY SENSOR

The possible usage of the MXene Ink for the production of the paper-based humidity sensors, was determined through the production of four different devices, composed of four different paper substrates. This way, both the impact of the ink layer and the influence associated with the paper substrates selected was analyzed. The employment of these different paper substrates implied changes in the device behavior, due to the different structural and chemical properties associated with each substrate. The ink spread tendencies, as well as the required time for adsorption, absorption, and desorption of water molecules from the cellulose structure was dependent on the substrate. On of the major reason for this phenomenon is associated with the chemical treatments the substrate may have been exposed to (notion applicable in the case of the office paper), and the varying weight, and associated porosity of each substrate. From Figure A5 it is possible to see the progressive reduction of the spacing set in between cellulose fibers, associated with a reduction in the porosity of each substrate.

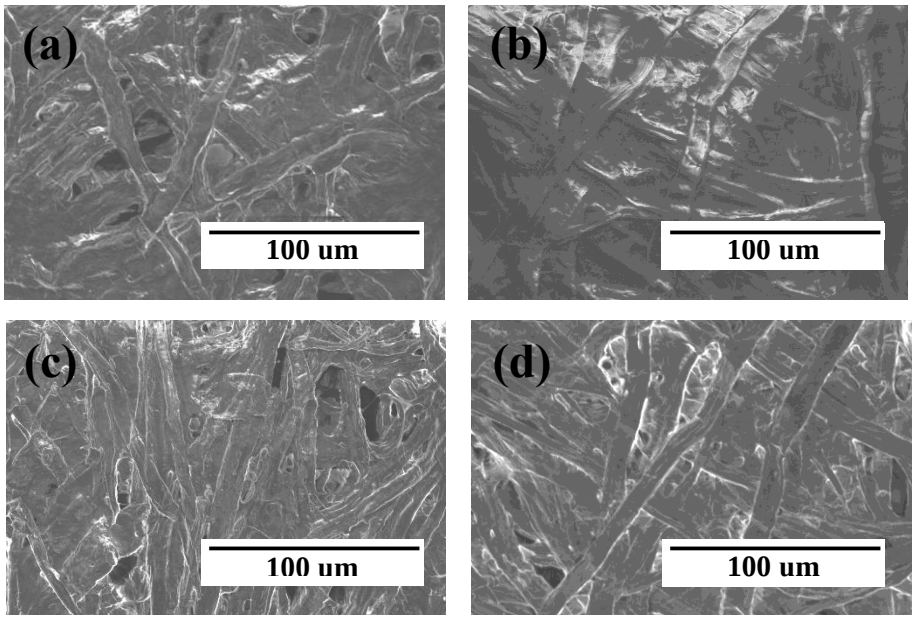

Figure B1 — Scanning Electron Microscopy (SEM) images of the paper-based substrates employed in the fabrication of the humidity sensors, at 500x magnification: (a) Navigator™ 40 g/m^2 sample; (b) Navigator™ 80 g/m^2 sample, (c) Navigator™ 100 g/m^2 sample, (d) Office paper 80 g/m^2 sample.

Similarly to the antenna analysis, the morphological properties of the deposited MXene ink layers were also attested through scanning electron microscopy (SEM). From the top-view associated with the samples associated with the different devices produced, the presence of the delaminated nanosheets evenly distributed can be observed, providing a complete and dense coverage of the device surface, as intended.

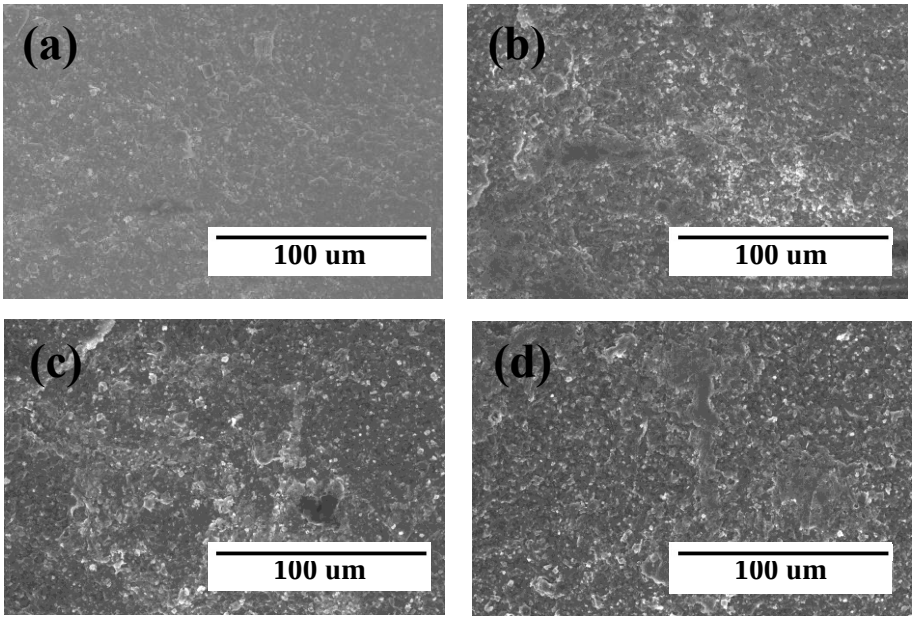

Figure B2 — Scanning Electron Microscopy (SEM) images of the deposited MXene layer pattern on top of the different humidity sensors tested, at 500x magnification: (a) Navigator™ 40 g/m^2 sample; (b) Navigator™ 80 g/m^2 sample, (c) Navigator™ 100 g/m^2 sample, (d) Office paper 80 g/m^2 sample.

In order to visualize the different layers, including the paper substrate, silver ink electrode, and the MXene ink layer, the cross-section of the Navigator 40 g/m^2 paper-based humidity sensor was also investigated through SEM imaging. In part due to damage through the cutting of the sample for observation, and possible extensive penetration of the silver ink within the cellulose structure, becomes difficult to clearly distinguish between the individual layers, assessing with exactness the thicknesses associated to which layer.

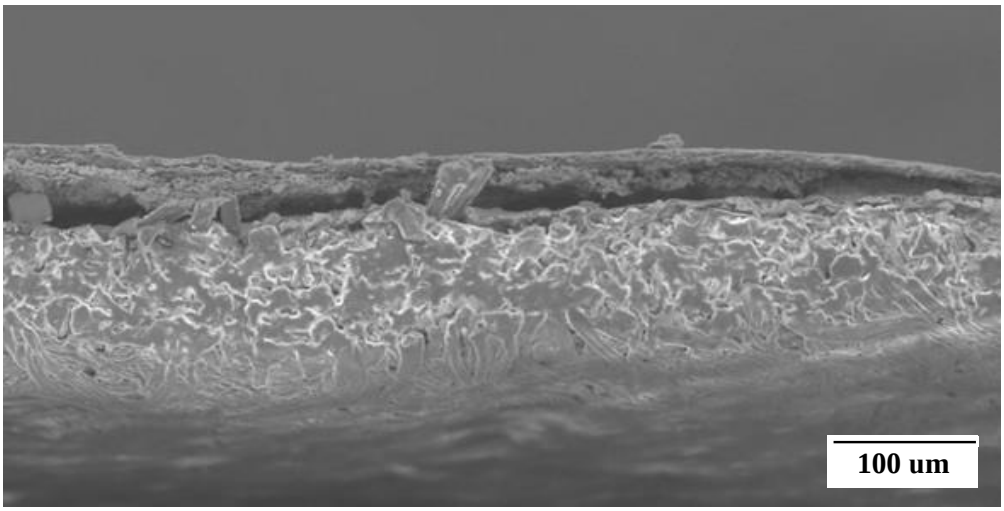

Figure B3 — Cross-section view of the Navigator™ 40 g/m^2 humidity sensor, at 200x magnification.